

# THE LUMINOSITY AND MASS FUNCTIONS OF LOW-MASS STARS IN THE GALACTIC DISK: I. THE CALIBRATION REGION\*

KEVIN R. COVEY<sup>1</sup>, SUZANNE L. HAWLEY<sup>2</sup>, JOHN J. BOCHANSKI<sup>2</sup>, ANDREW A. WEST<sup>3</sup>, I. NEILL REID<sup>4</sup>, DAVID A. GOLIMOWSKI<sup>5</sup>, JAMES R. A. DAVENPORT<sup>6</sup>, TODD HENRY<sup>7</sup>, ALAN UOMOTO<sup>8</sup>

DRAFT November 2, 2018

## ABSTRACT

We present measurements of the luminosity and mass functions of low-mass stars constructed from a catalog of matched Sloan Digital Sky Survey (SDSS) and 2 Micron All Sky Survey (2MASS) detections. This photometric catalog contains more than 25,000 matched SDSS and 2MASS point sources spanning  $\sim 30$  square degrees on the sky. We have obtained follow-up spectroscopy, complete to  $J=16$ , of more than 500 low mass dwarf candidates within a 1 square degree sub-sample, and thousands of additional dwarf candidates in the remaining 29 square degrees. This spectroscopic sample verifies that the photometric sample is complete, uncontaminated, and unbiased at the 99% level globally, and at the 95% level in each color range. We use this sample to derive the luminosity and mass functions of low-mass stars over nearly a decade in mass ( $0.7 M_{\odot} > M_{*} > 0.1 M_{\odot}$ ). The luminosity function of the Galactic disk is statistically consistent with that measured from volume complete samples in the solar neighborhood. We find that the *logarithmically binned* mass function is best fit with an  $M_c=0.29$  log-normal distribution, with a 90% confidence interval of  $M_c=0.20-0.50$ . These 90% confidence intervals correspond to *linearly binned* mass functions peaking between  $0.27 M_{\odot}$  and  $0.12 M_{\odot}$ , where the best fit MF turns over at  $0.17 M_{\odot}$ . A power law fit to the entire mass range sampled here, however, returns a best fit of  $\alpha=1.1$  (where the Salpeter slope is  $\alpha = 2.35$ ); a broken power law returns  $\alpha=2.04$  at masses greater than  $\log M = -0.5$  ( $M=0.32 M_{\odot}$ ), and  $\alpha=0.2$  at lower masses. These results agree well with most previous investigations, though differences in the analytic formalisms adopted to describe those mass functions, as well as the range over which the data are fit, can give the false impression of disagreement. Given the richness of modern-day astronomical datasets, we are entering the regime whereby stronger conclusions can be drawn by comparing the actual datapoints measured in different mass functions, rather than the results of analytic analyses that impose structure on the data *a priori*. Having validated this method to generate a low-mass luminosity function from matched SDSS/2MASS datasets, future studies will extend this technique to the entirety of the SDSS footprint.

*Subject headings:* Surveys – stars: late-type – stars: low-mass – stars: luminosity function – stars: mass function – Galaxy: stellar content

## 1. INTRODUCTION

The mass function (MF) is a fundamental property of stellar systems, describing the number of stars as a function of stellar mass. The MF is thus a statistical measure of the end result of the star formation process. Succinctly characterizing a stellar population, the MF also informs our understanding of the structure and dynamical evolution of stellar clusters, the Milky Way and other galaxies.

The first measurement of the MF was conducted by Salpeter (1955); for higher mass stars, this seminal re-

sult remains essentially unchanged to the present day. Salpeter found that the MF can be fit as a power law, formally expressed as:

$$\Psi(M) = \frac{dN}{dM} \propto M^{-\alpha} \text{ stars pc}^{-3} M_{\odot}^{-1} \quad (1)$$

where  $\alpha = 2.35$  is known as the ‘Salpeter slope’. Power law MFs which find a larger fraction of low-mass stars have larger values of alpha and are expressed as being ‘steeper’, while mass functions that find a lower fraction of low-mass stars have smaller values of  $\alpha$  and are described as ‘flatter’.

Other functional forms have been suggested to characterize the MF. In particular, a number of investigators (Miller & Scalo 1979; Chabrier 2005) present log normal MFs, which can be expressed as

$$\xi(M) = \frac{dN}{d \log M} = A \exp\left(\frac{-(\log M - \log M_c)^2}{2\sigma^2}\right) \quad (2)$$

Whichever functional form they adopt, most studies agree that the stellar MF appears to reach a peak at a few tenths of a solar mass. Power law characterizations of the MF require a flattening from a Salpeter slope for  $M > 1 M_{\odot}$  to  $\alpha \sim 0.5-1.7$  below  $1 M_{\odot}$ , while Chabrier (2005) finds a log-normal MF with a characteristic mass

\*BASED IN PART ON OBSERVATIONS OBTAINED WITH THE APACHE POINT OBSERVATORY 3.5-METER TELESCOPE, WHICH IS OWNED AND OPERATED BY THE ASTROPHYSICAL RESEARCH CONSORTIUM.

<sup>1</sup> Harvard-Smithsonian Center for Astrophysics, MS-72, 60 Garden Street, Cambridge, MA 02138; kcovey@cfa.harvard.edu

<sup>2</sup> University of Washington, Department of Astronomy, Box 351580, Seattle, WA 98195

<sup>3</sup> University of California Berkeley, Astronomy Department, 601 Campbell Hall, Berkeley, CA 94720-3411

<sup>4</sup> Space Telescope Science Institute, Baltimore, MD 21218

<sup>5</sup> Department of Physics and Astronomy, The Johns Hopkins University, 3400 North Charles Street, Baltimore, MD 21218-2686

<sup>6</sup> Department of Astronomy, San Diego State University, San Diego, CA 92182-1221

<sup>7</sup> Department of Physics and Astronomy, Georgia State University, Atlanta, GA 30302-4106

<sup>8</sup> Carnegie Observatories, Pasadena, CA, USA

of  $M_c=0.2$  is required to reproduce the stellar MF for a volume complete sample in the solar neighborhood. We refer the reader to comprehensive reviews by Scalo (1986), Reid & Hawley (2000), Kroupa (2002), Chabrier (2003), and Corbelli et al. (2005) for a more detailed understanding of the vast literature devoted to measuring the stellar MF.

Several processes have been advanced to explain the shape of the MF; examples include gravitational fragmentation (Klessen et al. 1998), competitive accretion (Larson 1992), truncation of mass accretion due to radiative or dynamical feedback (Silk 1995), star-star interactions (Reipurth & Clarke 2001) and the primordial distribution of clump masses within molecular clouds (Padoan & Nordlund 2002). The efficiency of each mechanism is influenced by physical variables, such as the metallicity and magnetic field strength of the parent molecular cloud, the local stellar density, and the intensity of the surrounding radiation field. These effects may ultimately result in observable MF variations as a function of environment, but at present the observed variations can be largely attributed to uncertainties arising from finite sample sizes and systematic differences in methodology (Chabrier 2005), though intriguing signs of MF variations with environment may be emerging (e.g., Taurus; Luhman 2004).

Previous studies of the Galactic disk MF have been limited, however, to samples of a few thousand low-mass stars (with low-mass stars defined for the purposes of this paper as  $M_* < 0.7 M_\odot$ ), due to the inability to simultaneously obtain a deep and wide photometric sample. Hawley et al. (2002) demonstrated that Sloan Digital Sky Survey (SDSS) and Two Micron All Sky Survey (2MASS) photometry of low-mass stars shows monotonic behavior across a wide range of colors. The accurate, multi-color catalogs produced by SDSS and 2MASS thereby allow the identification and characterization of millions of low-mass stars in the local Galactic neighborhood, enlarging previous photometric samples of field low-mass dwarfs by several orders of magnitude. The statistical power of such a sample makes an SDSS/2MASS catalog of low-mass dwarfs a promising avenue for improving our measurement of the low-mass stellar luminosity and mass functions.

To test and calibrate this technique before applying it to the entirety of the SDSS and 2MASS databases, we have performed a combined photometric and spectroscopic study of nearly 30,000 stars detected in  $\sim 30$  square degrees of overlap between the SDSS and 2MASS footprints. We describe in §2 the construction of this sample by matching the SDSS, 2MASS, and Guide Star Catalog (GSC) photometric databases. In §3 we present the spectroscopic follow-up of more than a third of the sample. We verify the completeness limit of the photometric sample in §4, where we also analyze the spectroscopic sample to understand the level of contamination and bias within the photometric catalog. We use this photometric catalog to measure the luminosity function of low-mass stars in the Galactic neighborhood in §5, derive a measurement of the low-mass stellar mass function in §6, and summarize our conclusions in §7. An appendix to this work presents native or transformed SDSS photometry for stars with measured trigonometric parallaxes, useful for constraining the empirical SDSS/2MASS

color-magnitude relation applied in §5.

We note that a full and complete description of our analysis necessarily results in a rather lengthy paper; we therefore suggest that many readers may wish to skip directly to §5 & 6 to concentrate upon the core scientific findings of this work, and then return to read §2, 3 & 4 if a deeper understanding of the assembly of the photometric sample and the effects of incompleteness, contamination and bias is desired.

## 2. A UNIFIED CATALOG OF SURVEY PHOTOMETRY

We analyzed SDSS, 2MASS, and GSC photometry for objects lying within a ‘calibration region’ defined as the area between right ascensions ( $\alpha$ ) of 3 and 15 degrees and declinations ( $\delta$ ) of -1.25 to +1.25 degrees. An abnormally large number of SDSS spectra of point sources were obtained in this region, allowing a test of the efficiency and robustness of the photometric sample assembled here (see §3.1). We excluded a small area [ $13.1 < \alpha < 13.3$ ,  $\delta < -1.05$ ] surrounding HD5112, a bright ( $V = 4.77$ ) M0 giant, which badly saturates SDSS photometry over a large area. The area of the calibration region thus subtends 29.957 square degrees on the sky.

### 2.1. Individual Survey Datasets

#### 2.1.1. Selecting 2MASS Stars

The Two Micron All Sky Survey (2MASS; Skrutskie et al. 2006) provides a homogeneous catalog in three near infrared filters ( $JHK_s$ ) ranging from 1 to 2.4  $\mu\text{m}$ . We queried the 2MASS All Sky Data Release (Cutri et al. 2003) via the GATOR interface<sup>9</sup> for all objects detected within the calibration region, retaining only objects with:

- astrometric location within the boundaries of the calibration region;
- high quality  $J$  band photometry (jphqual flag = ‘A’ or jrdfag = ‘1’ or ‘3’);
- unique detections of catalog objects (use-src flag = ‘1’);
- point source morphology (ext-key = ‘null’);
- no association with the predicted location of a known minor planet, comet, planet or planetary satellite (mp\_flg = 0).

These selection criteria generate a sample of 30,449 stellar candidates with IR detections within the calibration region.

#### 2.1.2. Selecting SDSS Stars

The initial mission of the SDSS was to map a quarter of the night sky centered on the North Galactic cap, acquiring accurate photometry of 100 million objects in 5 filters (Fukugita et al. 1996; Gunn et al. 1998) and accumulating over 1 million spectra (York et al. 2000). This mission is now complete, with over 9000 square degrees of photometry and over 1.25 million spectra released to the public in Data Release 6 (Adelman-McCarthy et al.

<sup>9</sup> <http://irsa.ipac.caltech.edu/applications/Gator/>

2008). SDSS observations were obtained with a dedicated 2.5 meter telescope at the Apache Point Observatory (Gunn et al. 2006). Photometric data were acquired as the telescope’s 3 degree field imaged in 5 filters ( $u, g, r, i, z$ ) nearly simultaneously by scanning a great circle across the sky at approximately the sidereal rate. Photometric data were reduced by a custom SDSS data processing pipeline (PHOTO ; Lupton et al. 2001) with calibrations obtained from observations by a 20-inch photometric telescope at the same site (Hogg et al. 2001; Smith et al. 2002; Tucker et al. 2006). The article describing the Early Data Release (Stoughton et al. 2002) provides information on the central wavelengths and widths of the SDSS filters, while papers discussing the “asinh” magnitude system (Lupton et al. 1999) and the SDSS standard star system (Smith et al. 2002) provide further information on the calibration of the SDSS photometric system. Astrometric precision and data quality assurance are also described by Pier et al. (2003) and Ivezić et al. (2004).

We assembled a catalog of stellar SDSS sources within the calibration region from imaging data first made public as Data Release 2 (Abazajian et al. 2004). SDSS stellar candidates satisfied the following criteria:

- SDSS astrometric location within 0.005 degrees (15-20”) of the calibration region (to allow matches for 2MASS objects whose proper motion may have carried them slightly out of the calibration region by the time of the SDSS imaging epoch);
- observed during a run which passed basic data quality tests (GOOD flag set);
- object represents the primary detection in the SDSS photometric database (PRIMARY flag set) to prevent multiple detections from overlap areas between adjacent SDSS runs;
- morphological identification as a point source (TYPE = 6).
- $i$  and  $z$  magnitudes above survey completeness limits ( $i < 21.1$ ,  $z < 20.3$ );
- no photometric processing flaws to ensure accurate photometry (SATURATED flag not set in either  $r$ ,  $i$  or  $z$ , PEAKCENTER flag not set, NOTCHECKED flag not set, DEBLEND-NOPEAK flag not set for an object with  $i$  psf error  $> 0.2$  magnitudes, PSF-FLUX-INTERP flag not set, BAD-COUNTS-ERROR flag not set, INTERP-CENTER and CR flags not both set);

These selection criteria identified 76,966 high quality SDSS detections of stellar candidates within this region; the last set of quality cuts removed 1486 stellar candidates, or  $\sim 1.9\%$  of the initial stellar catalog.

We note a subtle source of uncertainty in the SDSS  $z$  band photometry which may be of more importance for this study than for most other uses of the SDSS database. Spectral synthesis of L and T dwarfs (Burgasser, private communication) indicates that slight differences in the spectral response of the CCD detectors used for the  $z$  band observations can introduce  $z$  magnitude variations

up to 0.1 mags for early L through late T dwarfs. As we lack a robust characterization of this effect, and the vast majority of our sample is composed of K and M dwarfs for which this source of uncertainty is less important, we have not applied any  $z$ -band corrections to the survey photometry.

### 2.1.3. Selecting GSC Stars

The depth of the SDSS comes at the expense of a relatively faint saturation limit of  $i_{sat} \sim 14$ . This fixed apparent magnitude limit imposes a lower limit on the distance to SDSS stars with good photometric detections, and this distance limit is itself a function of the absolute magnitude of the star. Typical M0 dwarfs within 100 parsecs are saturated in SDSS imaging, for example, while M8 dwarfs only saturate in  $i$  for distances less than 10 parsecs. The 2MASS faint limit, however, restricted our sample to objects within 100 parsecs for objects of type M8 and later. Constructing a luminosity function of stars detected in both SDSS and 2MASS then required that early and late M dwarfs be sampled from disjoint physical volumes. As the calibration region is located at a Galactic latitude of  $-62$  degrees, this could potentially have introduced a bias in our analysis related to the scale height of the Galactic disk.

To include stars with saturated SDSS imaging in our catalog, we made use of GSC (version 2.2) optical photometry. The GSC (Space Telescope Science Institute & Osservatorio Astronomico di T 2001) is based on scans of photographic plates from the Palomar and UK Schmidt telescopes and provides star/galaxy morphological classification from measurements of 500 million objects in photographic  $B_J$  (as defined by Reid et al. 1991,  $\lambda \sim 4500 \text{ \AA}$ ) and  $R_F$  ( $\lambda \sim 6500 \text{ \AA}$ ) to a completeness limit of  $R_F \sim 18.5$ .

We assembled a catalog of GSC (version 2.2) objects brighter than a magnitude of 19.5 using the GSC data access page<sup>10</sup>, which we searched for morphological point sources (GSC Classification code = 0). These criteria identified 33,612 stellar candidates with GSC detections within the calibration region.

### 2.2. Creating a Matched Sample

To generate a comprehensive optical/near-infrared catalog of calibration region stars, we have merged the 2MASS, SDSS, and GSC stellar samples into a single matched catalog. As 2MASS photometry provides our only source of infrared observations, only objects with 2MASS detections were retained. 2MASS stars were matched to SDSS and GSC counterparts using a maximum matching radius of  $5''$ . We required unique matches – if an optical source was a potential counterpart for multiple NIR sources, only the closest association was preserved.

Of the 30,499 2MASS sources in the calibration region, 19,617 possessed both SDSS and GSC stellar counterparts. An additional 5265 and 4608 2MASS detections were identified with only a GSC or SDSS stellar counterpart, respectively. The final 959 2MASS stellar candidates ( $\sim 3\%$  of the input 2MASS sample) were not matched to counterparts in either optical catalog. Of

<sup>10</sup> [http://www-gsss.stsci.edu/support/data\\_access.htm](http://www-gsss.stsci.edu/support/data_access.htm)

these unmatched sources, 606 have  $15.2 < J < 16.3$ , and 753 have  $J < 16.3$ ; given the  $J = 16.2$  completeness limit of our catalog (see §4.1), this indicates that the bulk of these unmatched sources lie at the faint end of our sample, but still are confident detections. Visual analysis of SDSS imaging of the 753  $J < 16.3$  sources identified 73% (550/753) as galaxies: these objects were unresolved by 2MASS imaging, but resolved by the optical surveys, and were therefore not contained in the SDSS and GSC stellar catalogs.

The remaining 203 unmatched 2MASS sources brighter than  $J = 16.3$  were stellar sources, dominated by sources too faint for the GSC catalog and with sub-optimal SDSS photometry, and therefore excluded by the quality cuts described in §2.1.2. As these unmatched stellar sources represent a possible source of incompleteness in our final sample, we explore their properties in more detail in §4.1.

### 2.3. Recalibrating GSC Photometry

The 19,617 sources in common between the SDSS and GSC catalogs allowed an assessment of zero point errors in the GSC data. We calculated synthetic GSC magnitudes for SDSS sources using equations originally derived by Sesar et al. (2006), modified to account for local zero-point offsets:

$$B_{J,syn} = g + 0.279(g - r) + 0.06 \quad (3)$$

$$R_{F,syn} = r - 0.209(g - r) - 0.09 \quad (4)$$

The shape of the calibration region, 12 degrees wide in right ascension and only 2.5 degrees across in declination, implies that spatial gradients in imaging quality in right ascension are more important than gradients in declination, an expectation borne out in our dataset. The top panel of Figure 1 shows residuals between observed and synthetic GSC magnitudes as a function of right ascension. Assuming that the digital, drift-scanned SDSS data has a uniform zero point across the calibration region, these residuals reflect changes in photographic sensitivity across POSS plates. This expectation is supported by sharp discontinuities in the residuals on 5 degree spatial scales, the size of the POSS plates from which GSC magnitudes are measured.

To correct for spatial variations in the GSC zero point, we calculated the mean offset between synthetic and observed GSC magnitudes in 0.25 degree bins of right ascension. Applying this offset to all objects in that spatial bin produces recalibrated  $B_J$  and  $R_F$  magnitudes, corrected for the presence of the known zero-point error. Though these systematic zeropoint offsets are largely a function of right ascension, we have also repeated this process using 0.1 degree bins in declination. The result of this recalibration is illustrated in the bottom panel of Figure 1, which shows that large scale spatial gradients in the residuals have been removed.

We adopt characteristic errors for the recalibrated GSC magnitudes based on the remaining residuals between the recalibrated and synthetic GSC magnitudes. Gaussian errors with  $\sigma = 0.13$  accurately describe the recalibrated  $B_J$  residuals across the entirety of the calibration region. The recalibrated  $R_F$  residuals are well described by a Gaussian distribution with  $\sigma = 0.1$  magnitudes for  $\alpha > 8.2$ ; at  $\alpha < 8.2$ ,  $\sigma \sim 0.15$  is required to fit the bulk

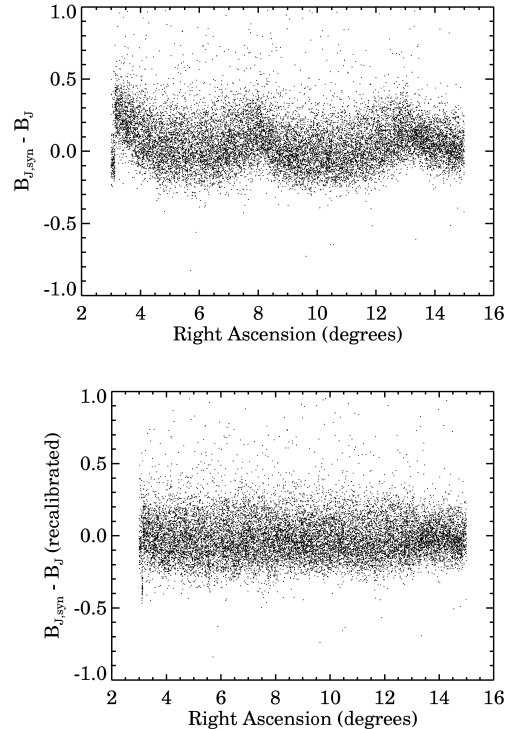


FIG. 1.— Residuals of observed and synthetic GSC  $B_J$  magnitudes calculated from SDSS photometry as a function of  $\alpha$  before (top) and after (bottom) recalibration with SDSS-based zero-points. The structure on 5 degree spatial scales in the top panel suggests that GSC magnitudes, measured from digitized POSS plates 5 degrees in size, contain systematic zero-point errors of the same order as the random photometric errors.

of the sources, and a tail of sources with large errors is still present. We thus conservatively assign errors of 0.2 magnitudes to recalibrated  $B_J$  magnitudes, and 0.15 magnitudes to recalibrated  $R_F$  magnitudes. Given the increased uncertainty of the  $R_F$  magnitudes for  $\alpha < 8.2$  degrees, we rely largely on  $B_J$  magnitudes in conducting our analysis.

### 2.4. Synthetic SDSS/2MASS Colors for GSC Sources

Measuring the luminosity and mass functions from photometric observations of the Galactic field requires the adoption of a color-magnitude relation to estimate the absolute magnitude, and ultimately mass, of each star. We used  $i - J$  for this purpose, as Hawley et al. (2002) have demonstrated that this color is a monotonic indicator of spectral type, and therefore temperature and luminosity, for late type dwarfs.

To create a sample of uniform  $i - J$  colors for the full photometric sample, we derived synthetic  $i - J$  colors for objects with observed  $B_J - J$  colors. Figure 2 shows the  $B_J - J$  and  $i - J$  colors for sources detected in both optical surveys. Interpolating the  $B_J - J$  colors of our sample onto the median trend of  $i - J$  as a function of  $B_J - J$ , we assigned each GSC/2MASS object that lacked bona fide SDSS data a synthetic  $i - J$  color. We estimated errors by combining in quadrature photometric uncertainties in  $B_J - J$  and the dispersion of the  $B_J - J$  vs.  $i - J$  relation.

Using the same methodology, we also derived synthetic  $i - z$  and  $r - i$  colors for all GSC sources with  $B_J - J$  colors. For GSC sources with only  $R_F$  magnitudes, we calculated the full suite of synthetic SDSS colors ( $i - J$ ,

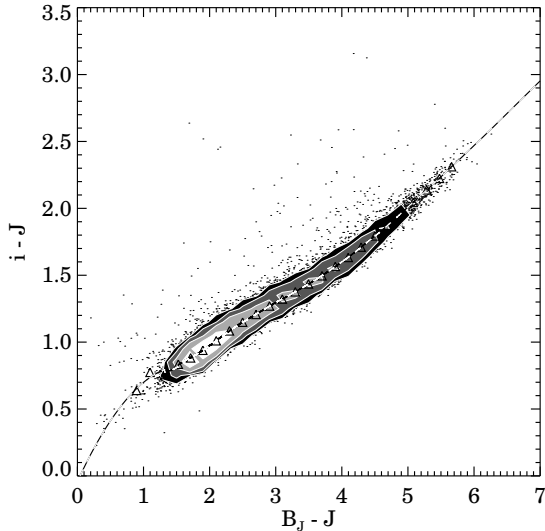


FIG. 2.—  $B_J - J$  and  $i - J$  colors for objects observed in both optical catalogs shown as black points and contours. The median  $i - J$  colors measured for 0.1 magnitude bins of  $B_J - J$  color are shown as triangles; the dashed line shows the function used to assign synthetic  $i - J$  colors as a function of  $B_J - J$  color to sources that lack SDSS data (e.g., saturated).

$r - i$ ,  $i - z$ ) using the same technique as applied to observed  $R_F - J$  colors. This minimizes the impact of the poorly recalibrated  $R_F$  photometry on our sample: only 232 objects are detected only in  $R_F$ ; all other sources have either native SDSS colors or synthetic colors generated from an observed  $B_J - J$  color.

### 3. SPECTROSCOPIC SAMPLE

We assembled an extensive database of follow-up spectroscopy to test for contamination (e.g., background giants, mis-identified QSOs, etc.) and bias (e.g., systemic misclassification of numerous M2 dwarfs as rarer M6 dwarfs due to dim, noisy photometry) in our photometrically selected sample of low-mass stars.

#### 3.1. SDSS Spectroscopy

SDSS spectroscopic observations were made with twin fiber-fed spectrographs, covering wavelengths from 3800Å to 9200Å with a spectral resolution of  $\lambda/\Delta\lambda \sim 1800$ . Each fiber was 3'' in diameter and plugged into a pre-drilled metal plate allowing observations across the 3 degree field of view of the SDSS telescope. A single plate accommodated 640 fibers, with 320 going to each spectrograph. The SDSS spectroscopic pipeline performed automated data reduction, producing flux calibrated spectra corrected for telluric absorption.

Each autumn, when the North Galactic Cap was completely inaccessible from Apache Point Observatory, SDSS-I focused its attention on an area along the celestial equator known as the Southern Equatorial Stripe, or Stripe 82. The observational projects conducted in Stripe 82 with the SDSS instruments during the autumn observing seasons included repeat imaging to allow investigations of SDSS data quality and to conduct time variability studies, as well as stand-alone observing programs proposed by collaboration scientists which had different targeting algorithms and data quality benchmarks than standard survey operations. Data products

generated by these observing programs were released as part of DR4, and are described in more detail by Adelman-McCarthy et al. (2006).

These additional datasets motivated us to place our calibration region in Stripe 82, as they contain thousands of stars with spectroscopic observations. Particularly useful to us were the SLoMaSS and ‘Spectra of Everything’ samples, described in full by Bochanski et al. (2007) and Vanden Berk et al. (2005). We identified stars in our sample with SDSS spectra using a 2'' matching radius between the position of each spectral fiber and the 2MASS position of each photometric object. Due largely to the two observing programs mentioned above, 10,784 stars in the calibration region, or more than a third of our matched sample, have an SDSS spectrum.

#### 3.2. Complete Observations

For two areas within the calibration region, covering one square degree in total, we acquired complete spectroscopic samples of low-mass stellar candidates. We refer to these areas as ‘complete region 1’ ( $4.19 < \alpha < 5.32$ ,  $-1.04 < \delta < -0.58$ ) and ‘complete region 2’ ( $11.68 < \alpha < 12.31$ ,  $-0.24 < \delta < +0.8$ ), and the union of the two as the ‘main complete’ sample. The ‘main complete’ samples include candidate late type dwarfs satisfying the following criteria:

- 2MASS astrometric positions within the boundaries of complete region 1 or 2;
- 2MASS photometry meeting the criteria expressed in §2.1.1, and  $J < 16$ ;
- SDSS or GSC counterparts meeting the selection criteria outlined in §2.1.2 or 2.1.3;
- Identification as a candidate late-type dwarf by one of the following two color-color cuts:
  - SDSS counterparts satisfying an  $r - i > 0.6 - 1.9(i - z)$  color-cut, encompassing the typical colors of late-type dwarfs identified by Hawley et al. (2002);
  - Objects lacking a high-quality SDSS counterpart but identified as candidate late-type dwarfs with a synthetic  $i - J > 1.2$  color cut. These candidates were only targeted in complete region 2, where the GSC photometry underpinning the synthetic  $i - J$  color is most reliable.

These cuts identified 536 targets for spectroscopic follow-up from an initial sample of 978 2MASS objects within the complete regions. The bulk of these objects (503) had SDSS counterparts meeting the criteria outlined in §2.1.2 for inclusion in this sample; a smaller number (33) had photometric flaws in SDSS, and we therefore resorted to synthetic, GSC-based magnitudes to characterize them.

To increase the statistics of this sample at the reddest colors, we expanded our criteria to cover larger areas of the sky, targeting candidates meeting the criteria for inclusion in ‘extended red’ and ‘super red’ samples. Candidates in these samples met the following criteria:

- 2MASS photometry meeting the criteria expressed in §2.1.1;
- Color and astrometric cuts:
  - the ‘extended red’ sample contains objects with 2MASS positions within  $-1.25 < \delta < 1.25$  and  $4 < \alpha < 6.5$  or  $11.5 < \alpha < 14$ , and  $i - z > 0.9$ ,  $i - J > 2.4$  and  $J < 15.8$ .
  - the ‘super red’ sample contains objects with 2MASS positions within the area defined by  $3 < \alpha < 15$  and  $-1.25 < \delta < 1.25$ , and  $i - J > 2.8$  and  $J < 16$ .

The union of the ‘main complete’, ‘extended red’, and ‘super red’ samples is a set of 672 candidate dwarf stars, of which 131 required spectroscopic observations with the ARC 3.5m telescope at APO. Table 1 documents the construction of each of these samples, listing the number of 2MASS sources that fell within the boundaries of each complete sample, the number that matched to SDSS and GSC sources, along with the subset that met the criteria for spectroscopic observation, and finally the number of 2MASS point sources with no point source counterpart in either SDSS or GSC. Table 2 breaks down the sources of the spectra in each sub-sample.

Finally, we note that SDSS spectra exist for many stars in Stripe 82 outside the boundaries of the complete regions, and 60 ARC 3.5m spectra were also obtained prior to the definition of the boundaries of the complete regions. We include these incompletely (though still densely) sampled sources in Table 2 under the ‘Other’ category, and used them to provide additional constraints on the quality of the photometric sample.

Using the Dual Imaging Spectrograph (DIS) on the ARC 3.5 meter telescope at Apache Point Observatory, we obtained spectra of 191 candidate late type dwarfs in the calibration region that lacked SDSS spectra. The DIS spectrograph simultaneously and independently records spectra at blue and red optical wavelengths using a dichroic beamsplitter centered at 5550 Å. Our observations used the ‘low’ blue and ‘medium’ red gratings and a 1.5 arcsecond (3 pixel) slit, providing wavelength coverage from 3800 Å to 8700 Å with a typical spectral resolution of  $\sim 700$  in the blue and  $\sim 1000$  in the red. Each DIS spectrum was reduced with a reduction script written in Pyraf, the Python-based command language for the Image Reduction and Analysis Facility<sup>11</sup>. All spectra were trimmed, overscan and bias corrected, cleaned of cosmic rays, flat fielded, extracted, dispersion corrected, and flux calibrated using standard IRAF tasks.

#### 4. QUALITY CHECKS

Measuring the luminosity and mass functions of low-mass stars from a purely photometric catalog requires a sample of the utmost quality. In particular, past efforts have often been waylaid by the effects of incompleteness (failing to detect all stars within the adopted completeness limit), contamination (incorporating objects other

than main sequence late-type dwarfs in the photometrically selected sample), and bias (color-dependent errors in detection efficiency or source classification). We used our photometric and spectroscopic observations to constrain the impact of these effects on our sample.

#### 4.1. Completeness

Incompleteness in our sample would lead to a systematic underestimate of the true physical density of stars in the Galaxy. Given the relative depths of the 2MASS and SDSS surveys, and the optical/NIR colors typical of low-mass stars, the inclusion of stars in our final sample depends primarily on the 2MASS sensitivity at faint magnitudes. This expectation is borne out by the results of the catalog matching described in §2.2; the vast majority ( $> 99\%$ ) of 2MASS detections match to an optical counterpart. The few which do not match, however, represent a second possible source of incompleteness in our final matched sample. Below we describe tests of the completeness of our sample, performed by empirically deriving the faint limit of 2MASS in the calibration region and studying the population of unmatched NIR sources.

##### 4.1.1. The Completeness Limit of the 2MASS survey

The canonical 2MASS 99% completeness limit is  $J = 15.9$  (Cutri et al. 2007), applicable over the entirety of the 2MASS catalog except in areas where source confusion is the primary cause of non-detections. As the calibration region probes high ( $|b| > 50$ ) Galactic latitudes, stellar density is low enough that observational sensitivity is the main source of incompleteness. Variations in seeing, airglow intensity, and system zeropoints, however, result in individual 2MASS tiles possessing true completeness limits up to a magnitude fainter than the canonical value. Deeper SDSS observations, however, allow a direct measurement of the magnitude at which 2MASS becomes incomplete.

To test the completeness limit of 2MASS in the calibration region, added an estimate of each star’s  $i - J$  color, derived from a least squares quadratic fit to the median  $i - J$  vs.  $i - z$  relation for sources with both SDSS and 2MASS detections, to their measured  $i$  magnitudes, producing a synthetic  $J$  magnitude ( $J_{syn}$ ) for each SDSS star. Comparing  $J_{syn}$  to the actual  $J$  magnitude observed from bona fide 2MASS detections revealed that  $J_{syn}$  is accurate to within  $\sim 0.1$  magnitudes (median error = 0.05 magnitudes,  $\sigma = 0.13$  magnitudes).

Figure 3 compares the distribution of  $J$  magnitudes measured in the matched 2MASS/SDSS sample with the distribution of  $J_{syn}$  values estimated for all SDSS sources in the calibration region, demonstrating that the matched 2MASS/SDSS sample becomes incomplete at  $J = 16.3$ . Given the  $\sim 0.1$  mag. uncertainties in  $J_{syn}$ , we select  $J = 16.2$  as a conservative estimate of the 2MASS completeness limit in the calibration region.

Applying a  $J < 16.2$  completeness limit to our catalog reduced the number of 2MASS stellar candidates to 26,585. Of these candidates, 20,869 matched to SDSS counterparts and 23,099 matched to GSC counterparts, with 18,012 candidates matched to counterparts in both catalogues.

##### 4.1.2. Understanding Unmatched 2MASS sources

<sup>11</sup> PyRAF is a product of the Space Telescope Science Institute, which is operated by AURA for NASA. IRAF is distributed by the National Optical Astronomy Observatories, which are operated by the Association of Universities for Research in Astronomy, Inc., under cooperative agreement with the National Science Foundation.

TABLE 1  
 SELECTING THE COMPLETE SAMPLES

Sample	2MASS sources in footprint	SDSS counterpart Total	SDSS counterpart Spectra	GSC counterpart Total	GSC counterpart Spectra	No optical counterpart
Main Complete	978	765	503	201	33	12
Extended Red	9654	7382	101	2182	3	90
Super Red	20499	15957	32	4246	0	296

 TABLE 2  
 SPECTROSCOPIC OBSERVATIONS

Sample Sample	SLoMaSS Spectra	Misc. SDSS Spectra	APO Spectra	Visually Rejected
Main Complete	421	15	100	0
Extended Red	73	12	19	0
Super Red	7	10	12	3
Other	7354	2892	60	0
TOTAL	7855	2929	191	3

 TABLE 3  
 SDSS FLAGS FOR COUNTERPARTS OF UNMATCHED  
 2MASS SOURCES

Stars Affected	Photometric Flaw
73	SATURATED
53	PSF-FLUX-INTERP
22	dubious GALAXY classification
17	NOTCHECKED
13	not PRIMARY
8	PEAKCENTER
3	INTERCENTER
2	undetected by PHOTO
1	satellite track
9	2MASS diffraction spike
2	2MASS false detections

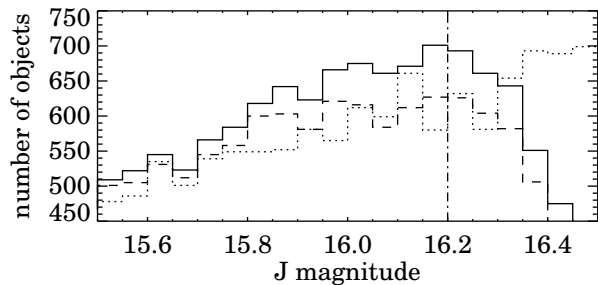
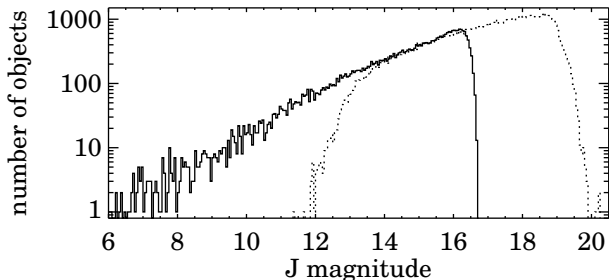


FIG. 3.— Top: The number of 2MASS sources detected in the calibration region (solid black line) vs.  $J$  magnitude compared to the number predicted on the basis of SDSS detections (dotted line). Bottom: As above, focusing on the faint limit of the 2MASS survey. Indicated are the adopted  $J = 16.2$  2MASS completeness limit (dot-dashed line), and the number of 2MASS sources matched to optical counterparts (dashed line). The presence of faint 2MASS ‘orphans’ is revealed by the gap between the solid and dashed lines; these sources are discussed in §4.1.2.

The 753 2MASS sources in the calibration region with  $J < 16.3$  and no optical counterpart represent a second potential source of incompleteness. To understand the nature of these unmatched sources, we visually inspected their SDSS and 2MASS imaging. As noted previously in §2.2, 550 were galaxies; these objects correctly had no counterpart in our optical catalogs of point sources. Of the remaining 203, only 11 appear to be spurious 2MASS detections: nine due to the mistaken identification of a bright star’s diffraction spike as an independent photometric object, and two due to identifying random sky

noise fluctuations as objects.

The remaining 192 objects appear to be genuine detections of point sources, but whose SDSS counterpart does not meet the quality cuts discussed in §2.1.2. Table 3 summarizes the photometric flaws preventing 2MASS sources from matching to optical counterparts in the SDSS catalog. We exhaustively investigated these unmatched stars, and provide a brief summary of the most relevant details below. Curious readers can find a full description of this inquiry presented in Covey (2006).

SDSS counterparts for 73 of the 192 unmatched stars were eliminated from our sample due to the SATURATED flag being set; counter-intuitively, these were typically faint stars, but located within the PSF wings of a saturated star. The bulk of the remaining unmatched 2MASS sources possessed SDSS counterparts with sub-standard imaging, either due to random noise (cosmic rays) or instrumental effects (landing on a bad CCD column, etc). These flaws, indicated by the PSF-FLUX-INTERP, NOTCHECKED, PEAKCENTER, and INTERCENTER flags, accounted for another 81 of the 192 2MASS stars unable to match to their SDSS counterpart. The remaining 38 sources were excluded either because PHOTO identified them as extended objects (often affecting members of a marginally resolved visual binary), because they were subject to extremely rare photometric errors (sources eluding identification by PHOTO, or contamination of the star’s PSF by the path of a satellite).

The Guide Star Catalog, an independent set of optical measurements, should protect against the loss of stars from the sample due to SDSS photometric errors. Sub-standard DR4 photometry indicates that the majority of these sources (114/186) are too dim ( $r < 18.5$ ) to be properly detected in the Guide Star Catalog. The remaining 72 sources are typically bona fide bright stars or close binaries with a marginally saturated component – the saturation contaminates both SDSS detections, while

the pair is unresolved in GSC imaging.

The tendency for unmatched 2MASS sources to possess faint and red counterparts in substandard SDSS photometry suggests our matching algorithm may be biased against the latest type stars. To quantify this effect, we compared  $i - J$  colors for sources with substandard SDSS detections to those of the full SDSS/2MASS matched sample. Sources with substandard SDSS detections are skewed towards redder  $i - J$  colors than the full SDSS/2MASS sample, but represent less than 6% of all sources for all but the reddest colors ( $i - J \sim 2.6$ , where small number statistics [ $n_{stars}/bin=3$ ] dominate).

From this analysis, we conclude that the sample is more than 99% complete to  $J = 16.2$ , and more than 94% complete for every color where  $i - J < 2.6$ . Photometric flaws in SDSS imaging marginally affect the completeness of faint sources without GSC counterparts; coupled with the NIR magnitude limit of this sample, this effect may introduce a small color-dependent bias into our sample, such that we underestimate the true density of the reddest stars at the 20% level.

#### 4.2. Spectroscopic Quality Tests

Using the spectroscopic catalog described in Section 3, we placed empirical limits on the contamination of our photometric catalog by objects other than low-mass dwarf stars. Additionally, we tested for bias within our sample, ensuring that photometric colors accurately predict spectral types (and thus luminosities and masses) of late type dwarfs in our catalog. Unresolved binary systems represent a particularly important source of bias for this study, and as such we discuss them separately in §5.4.

##### 4.2.1. Identifying Exotic Contaminants

We began our spectroscopic analysis by assigning spectral types to each spectrum, using the ‘Hammer’ spectral typing software. This set of IDL routines uses 28 spectral indices to estimate the spectral type of an input spectrum, and then allows the user to modify the assigned type via visual comparison to a grid of dwarf standards. The automated spectral typing algorithm has been tested with template spectra degraded to  $S/N \sim 4$ , returning results accurate to  $\pm 2$  subclasses. Tests of spectral types interactively assigned by multiple users agree to within one subclass. For a full description of the Hammer algorithm, we refer readers to appendix A of Covey et al. (2007)<sup>12</sup>.

Using the Hammer, we assigned spectral types to the vast majority of the spectra in our sample. Of the 669 spectra in the Main Complete, Extended Red, and Super Red spectroscopic samples, only one object could not be confidently assigned a stellar spectral type; it contained spectral features from both a white dwarf and an M dwarf component. These unresolved white dwarf-M dwarf (WDMD) binary systems have proven to be relatively abundant in the SDSS spectroscopic database (Silvestri et al. 2006).

<sup>12</sup> The Hammer has been made available for community use and can be downloaded from [http://www.cfa.harvard.edu/~sim\\$kcovey/thehammer](http://www.cfa.harvard.edu/~sim$kcovey/thehammer), and/or from the tarfile provided by Covey et al. (2007) to the *AJ* to be archived with the electronic edition of their article

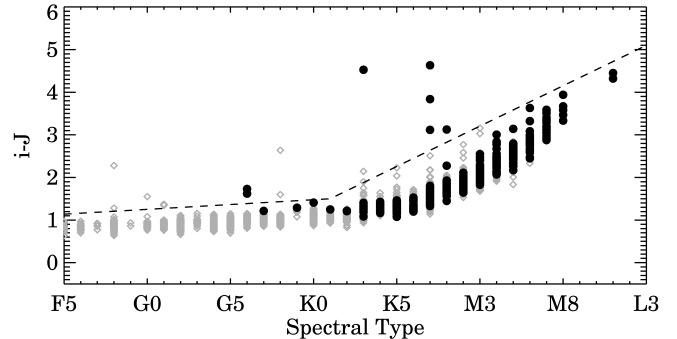


FIG. 4.— Assigned spectral types as a function of photometric  $i - J$  color (either directly measured from SDSS/2MASS photometry, or transformed from GSC/2MASS photometry). Grey diamonds denote all calibration region objects with spectra and  $J < 16.2$ , while black circles indicate members of the complete spectroscopic samples. The dashed line demonstrates a cut to identify sources whose photometry and spectral types disagree significantly.

Similarly, of the 9649 sparsely sampled spectra with counterparts brighter than  $J = 16.2$ , all but 24 were assigned stellar spectral types. Of the 24 non-stellar spectra, three were too noisy to confidently estimate a spectral type, and seven revealed additional WDMD pairs. The remaining 14 spectra revealed more exotic contaminants: four carbon stars, six unresolved galaxy populations (i.e. galactic bulges or clusters), and four QSOs. The QSOs, as well as the seven WDMD pairs, fall within the  $u - g < 1$  and  $g - r < 1.1$  region that contains more than 95% of the QSOs in the SDSS Quasar Catalog (?). The galactic populations and carbon stars lie within the stellar locus, unidentifiable by photometry alone. Extending our analysis to the 1326 additional spectra fainter than  $J = 16.2$  revealed 11 more objects without stellar spectral types. The majority (nine) of these objects were QSOs, while two objects were simply too noisy to confidently assign a spectral type.

In total, analysis of the 10,975 spectra within our sample revealed 35 objects which cannot be assigned a stellar spectral type, implying a global contamination rate of 0.3% for our matched sample. More than half (20/35) of these exotic contaminants, however, can be eliminated by restricting our sample to objects outside the  $u - g < 1$  and  $g - r < 1.1$  region. Similarly, Ivezić et al. (2002) identified a  $g - i$  vs.  $i - K_s$  color-color cut which can also help to distinguish stars from QSOs.

##### 4.2.2. $i - J_{2MASS}$ as a Spectral Type Indicator

Figure 4 displays spectral types of stars in our sample as a function of  $i - J$  color. Consistent with previous studies (Hawley et al. 2002; West et al. 2005), we found that  $i - J$  predicts spectral type reliably in the M and K spectral classes. The typical spread of  $i - J$  at a given spectral type is  $\sim 0.1$  mag, though there is a slight color dependence; the standard deviation of  $i - J$  increases from 0.07 mag for G5 stars to 0.12 mag for M3 stars.

While the vast majority of the sample shows a well-behaved color vs. spectral type relation, there are stars with  $i - J$  colors significantly redder than other stars of the same spectral type. For our purposes, stars with late K and early M spectral types but  $i - J$  colors typical of late M and early L types are of the most concern. With only a small number of bona-fide late M and early L type

objects in our sample, consistently misclassifying even a small fraction of the earlier type stars could significantly inflate the luminosity and mass functions at the lowest masses.

To investigate the cause of these color/spectral type discrepancies, we inspected 20 sources with  $i - J$  colors significantly redder than other stars of the same spectral type (this cut is shown as a dashed line in Figure 4). Four of these sources were early type F and G stars that saturated the SDSS, and their anomalous  $i - J$  colors, more typical of late K/early M stars, are likely due to the larger errors of synthetic  $i - J$  colors calculated from GSC photometry. Given the large number of bona fide late-K/early-M objects in our sample, and the low incidence of mis-classified saturated SDSS stars (4/10,940 stars in the complete spectroscopic sample), this effect will have a negligible impact on our analysis.

The remaining 16 sources with anomalous  $i - J$  colors are due to difficulties in properly associating SDSS and 2MASS sources into a matched catalog. One such mismatch is SMSS (Sloan M Star Survey) J003716.5+000106.4; with the PSF-FLUX-INTERP flag set in the SDSS detection of this object, our algorithm incorrectly identifies a nearby faint star as this object's SDSS counterpart, resulting in a non-physical matched detection with an extremely red  $i - J$  color. Due to the differing spatial resolutions of the two surveys, visual binaries with small ( $\leq 1.5''$ ) separations were often resolved into distinct objects by SDSS, but not by 2MASS. This scenario also results in an anomalously red  $i - J$  color, as the  $i$  band flux is being derived from a single component of the system, while the  $J$  band flux is the sum of both components.

Given the relative scarcity of objects with true  $i - J$  colors  $\geq 3$ , these mismatches could artificially double the number of objects in the reddest bins of our luminosity and mass functions. We eliminated such mismatches from our sample, however, by requiring that the SDSS and SDSS/2MASS properties of each detection are self-consistent. Figure 5 shows a simple  $i - z$  vs.  $i - J$  color cut ( $i - z < i - J * 0.574 - 0.738$ ;  $i - z < 1.5$ ) that we used to remove these mismatches from our sample.

#### 4.2.3. Kinematically Selected Subdwarf Candidates

We estimated the number of subdwarfs in our photometric sample by identifying objects with proper motions indicative of halo kinematics. Such objects can be found photometrically using the reduced proper motion,

$$H_r = r + 5 + 5 \log \mu \quad (5)$$

for a star with magnitude  $r$  and proper motion  $\mu$ , expressed in arc seconds per year. Preliminary proper motions measured from the USNO-B and SDSS catalogs produce the reduced proper motion diagram shown in Figure 6 for objects in the calibration region with SDSS counterparts and  $> 3 \sigma$  detections of proper motion (corresponding to a proper motion limit of  $1''/\text{century}$ ; Munn et al. 2004), or more than a third of the objects in the photometric sample (12022/30449). The disk population dominates this diagram, but a spur of objects with reduced proper motions lying significantly below the disk locus is clearly seen. We isolated candidate subdwarfs within this spur as objects with  $(r - i) > 0.1$  and

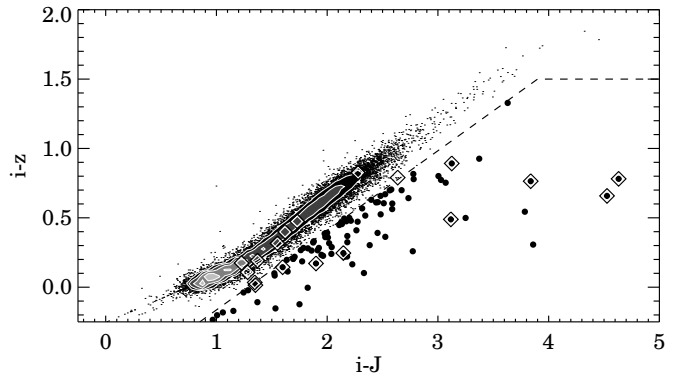


FIG. 5.— Mismatched SDSS and 2MASS detections in  $i - z$  vs.  $i - J$  color-color space. Black points and greyscale contours show the colors of the entire photometric sample. Sources identified in the full spectroscopic sample as possessing discrepant  $i - J$  colors and spectral types are shown with nested black and white diamonds. Sources with discrepant  $i - J$  colors and spectral types that fall in the middle of the  $i - z$  vs.  $i - J$  stellar locus typically lack reliable SDSS detections, and have synthetic  $i - J$  and  $i - z$  colors estimated from GSC photometry and are thus consistent with the stellar locus by construction. Sources with  $i - J$  colors redward of the dashed line are likely mismatches, and are shown as filled circles.

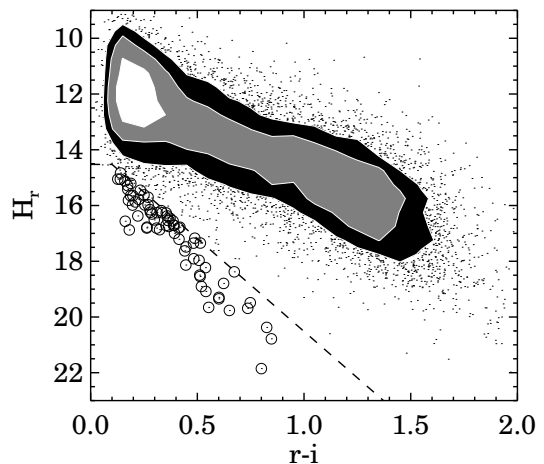


FIG. 6.— Reduced proper motion ( $H_r$ ) vs.  $r - i$  for calibration region stars with SDSS colors and  $\mu > 1''/\text{century}$ . Objects with thin/thick disk kinematics are shown as black points and contours; subdwarf candidates are highlighted with open circles. The  $(r - i) > 0.1$  and  $H_r > 13.86 + 6.666*(r - i)$  subdwarf selection criteria is shown as a dashed line.

$H_r > 13.86 + 6.666*(r - i)$ , identifying 0.5% (69/12022) of SDSS/2MASS objects with well-measured proper motions as candidate subdwarfs.

The colors of these candidates buttress their status as subdwarf candidates. These kinematically selected candidate subdwarfs are  $\sim 0.1$  mag. bluer in  $u - g$  than typical dwarfs with similar  $g - r$  colors, consistent with the  $U - B$  ‘ultraviolet excess’ previously observed for subdwarfs (see Bessell & Wickramasinghe 1979, Figure 2). The 10 coolest ( $r - i > 0.55$ ) candidate subdwarfs also show a redward shift in  $g - r$ , consistent with the trend observed by West et al. (2004) in their sample of spectroscopically selected SDSS candidate subdwarfs.

We note that the 0.5% subdwarf contamination rate implied by this kinematically selected sample overestimates the fraction of subdwarfs present in our sample. The large space velocities of subdwarfs make them more

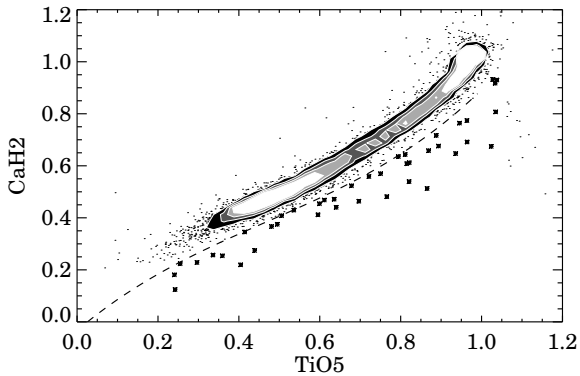


FIG. 7.— Measurements of the TiO5 and CaH2 indices defined by Reid et al. (1995). Black points and grayscale contours show the values measured from the subset of our sample with spectroscopic observations. The dashed line shows the boundary defined by Gizis (1997) to separate subdwarfs from solar metallicity stars. Objects identified as candidate subdwarfs by this cut are shown as asterisks.

likely than slower moving disk dwarfs to fulfill a  $3\sigma$  cut on proper motion. Indeed, our 0.5% subdwarf contamination rate implies a local normalization of the disk and halo populations at the 200:1 level, a factor of two larger than the accepted value (Reid & Hawley 2000).

#### 4.2.4. Spectroscopically Identified Subdwarf Candidates

M subdwarfs can also be identified by comparing the strength of metallicity sensitive spectral features, such as CaH and TiO (Gizis 1997). Unfortunately, no similarly broad features exist to identify G and K subdwarfs with spectra of moderate resolution and signal-to-noise (Morell 1988).

We identified late-type subdwarfs in our sample by measuring the TiO5 and CaH2 indices defined by Reid et al. (1995) for our spectroscopic sample. The resulting TiO5 vs. CaH2 diagram is shown in Figure 7, along with the polynomial fit defined by Gizis (1997) to select M type subdwarfs. Detailed abundance analyses by Woolf & Wallerstein (2005) suggest that the subdwarf boundary defined by Gizis (1997) identifies late type stars with  $[\text{Fe}/\text{H}] \sim -0.5$  dex or below.

Within the full spectroscopic sample, 41 stars were identified as candidate subdwarfs by their TiO5 vs. CaH2 ratio. Visual inspection led us to discard 22 of these sources with noisy or flawed spectra, leaving 19 candidate low metallicity M dwarfs. Of 546 M stars in the complete spectroscopic sample, only one was identified as a candidate late type subdwarf, representing an M star subdwarf contamination rate of 0.18%. Similarly, of the 7593 M stars in the full spectroscopic sample, the 19 candidate late type subdwarfs represent a 0.25% contamination rate. Combining these results with the  $\sim 0.5\%$  subdwarf fraction implied by the kinematic analysis in §4.2.3, it appears that subdwarf/halo stars make up less than 0.75% percent of a matched SDSS/2MASS sample of late-type stars.

#### 4.2.5. Giant Stars

Evolved stars, with effective temperatures and colors similar to main sequence stars, represent a particularly important source of contamination to a photometric catalog of main sequence stars. Since giants are much more luminous than dwarfs, a given flux limit for observational detection implies a larger distance limit for

giants than for main sequence dwarfs of the same color; effective distance limits for giants are typically 50 times larger, such that a survey is sensitive to giants over a volume more than 100,000 times greater than that for dwarf stars. Thus, while the absolute space density of giants is low, they can make up a significant component of a magnitude limited sample of point sources.

Bessell & Brett (1988) and Worthey & Lee (2006) have identified the  $JHK_s$  and  $VIK_s$  color spaces (see their Figs. 5 and 4, respectively) as particularly useful for separating late-type dwarfs and giants. Given the size of the expected  $JHK$  color shifts ( $\sim 0.2$  mag) relative to the accuracy of the 2MASS photometry, we can only draw the general conclusion that the sample is dominated by dwarf stars; in our sample,  $J-H$  becomes noticeably bluer redward of  $H-K_s \sim 0.15$ , with no distinct plume of giant stars extending towards  $J-H \sim 1$  at  $H-K_s \sim 0.15$ . Very few stars in the calibration region have  $giK_s$  colors indicative of giants, and the tens of objects that do make up a very small percentage of the total number of sources detected at that  $i-K_s$  color.

Spectroscopic indices allowed us to identify G and K giant candidates within our sample, producing an empirical estimate of their effect on our analysis. Using 2388 spectra from numerous spectral libraries (Torres-Dodgen & Weaver 1993; Danks & Dennefeld 1994; Fluks et al. 1994; Lançon & Wood 2000; Prugniel & Soubiran 2001; Bagnulo et al. 2003; Le Borgne et al. 2003; Bochanski et al. 2007), we tested spectroscopic indices that identify giant stars in moderate resolution, moderate signal to noise spectra (Malyuto et al. 1997; Malyuto & Schmidt-Kaler 1999). These indices are given in Table 4, with each index calculated as a ratio of the mean flux in the spectral regions identified as the index numerator and denominator. The only exception is the  $\text{Mg}_2$  index, which was calculated as a pseudo-equivalent width, consistent with its original definition in Morrison et al. (2003).

We used  $\text{Mg}_2$  vs.  $g-r$  as our primary giant/dwarf discriminant (Morrison et al., in prep; Yanny et al., in prep.). At red  $g-r$  colors, however, the dwarf and giant sequences reconnect. To identify even the reddest giant stars, we selected giant candidates from this confused region of  $\text{Mg}_2$  vs.  $g-r$  space using three supplementary spectroscopic criteria ( $\text{Na D } 5900$  vs.  $\text{Mg b}$ ;  $\text{TiO } 6700$  vs.  $\text{Blend } 6497$ ;  $\text{CN } 7900$  vs.  $\text{Na D } 8200$ ) to reject likely late type dwarfs. This technique identified 104 candidate giants from 8750 objects in our sample with both  $g-r$  colors and spectra, representing a 1% global giant contamination rate.

To test if these spectroscopically identified candidate giants are consistent with standard models of the stellar population of the Milky Way, we generated simulated SDSS/2MASS observations using the TRILEGAL code (Girardi et al. 2005). The top two panels of Figure 8 show the locations of giant stars in  $i-J$  vs.  $J$  color-magnitude space as predicted by the TRILEGAL simulation using standard Galactic parameters and the location of the calibration region (top left panel) and as identified in our spectroscopic sample (top right panel). The TRILEGAL simulation predicts that giants should reside in a relatively narrow locus in  $i-J$  vs.  $J$  color-magnitude space stretching from  $J \sim 6$  and  $i-J \sim 1.3$  down to  $J \sim 16$  and  $i-J \sim 1.0$ . The locations

TABLE 4  
SPECTRAL INDICES FOR DWARF/GIANT DISCRIMINATION

Band name	Numerator 1	Numerator 2	Denominator	Reference
Mg <sub>2</sub>	4935 – 4975	5303 – 5367	5130 – 5200	Morrison et al. (2003)
Mg b	5100 – 5150	5320 – 5420	5150 – 5320	Malyuto et al. (1997)
Na D 5900	5789 – 5839	6020 – 6120	5839 – 6020	Malyuto et al. (1997)
Blend 6497	6406 – 6470	6582 – 6637	6470 – 6536	Malyuto & Schmidt-Kaler (1999)
TiO 6700	6425 – 6525	6970 – 7040	6613 – 6832	Malyuto et al. (1997)
CN 7900	7815 – 7887	7970 – 8037	7887 – 7970	Malyuto & Schmidt-Kaler (1999)
Na D 8200	8120 – 8170	8210 – 8260	8170 – 8210	...

of our spectroscopically identified candidate giant stars in  $i - J$  vs.  $J$  color-magnitude space match these predictions well; though the spectroscopic catalog only contains sources with relatively faint  $J$  magnitudes, Figure 8 shows the faint spectroscopically identified giant star candidates are indeed concentrated about  $i - J \sim 1.1$ . Additionally, the photometric sample shows a distinct plume of sources tracking the expected giant star locus, most prominently at  $J \sim 11$  and  $i - J \sim 1.2$ .

The bottom panels of Figure 8 show histograms of the  $i - J$  colors of all stars, as well as just giants, in both the TRILEGAL simulation and the observed data. The TRILEGAL simulation predicts a global contamination rate for our sample of 4%, but this is a strong function of color, with giant star contamination rising above 10% blueward of  $i - J \sim 1.15$ . We drastically reduced giant star contamination by restricting our analysis to sources with  $J > 12$  and  $i - J > 1.25$  ( $> K5$ ), bounded in Figure 8 by blue dashed lines. These cuts reduce giant star contamination to a negligible level (less than 2% in the bluest, most contaminated color bin) while sacrificing only a handful of bona fide low-mass dwarf stars.

## 5. THE LUMINOSITY FUNCTION

The previous section demonstrates that we can construct a matched SDSS/2MASS dataset for stars with  $12 < J < 16.2$  and  $1.25 < i - J < 4.5$  where incompleteness, contamination, and bias are limited to  $\leq 1\%$  for the full sample, and  $< 5\%$  for stars in a small ( $\sim 0.1$  mag) color range. We are thus confident in the quality of the calibration region data, and now describe the use of this dataset to measure the luminosity and mass functions of the Galactic disk.

Beginning with the combined photometric sample assembled in §2, we culled the catalog to ensure completeness and reduce contamination and bias from background giants and bad matches. In doing so, we restricted our analysis to only those sources meeting the following additional color and magnitude criteria:

- completeness cut:  $J < 16.2$  & SDSS or GSC optical counterpart (leaves 25,947 candidates);
- giant contamination cut:  $J > 12$  &  $i - J > 1.25$  (leaves 13,159 candidates);
- bad match cut:  $i - z < 1.5$  &  $i - z > 0.574(i - J) - 0.738$  (leaves 13,088 candidates)
- QSO/WDMD contamination cuts<sup>13</sup>:  $u - g > 1$  or

<sup>13</sup> The need for  $u - g$  colors to implement these cuts restricts their usage to only those objects with SDSS optical counterparts.

$g - r > 1.1$  or  $i - K < 1.5 + 0.8 * (g - i)$  (leaves 13,064 objects in final sample).

We will refer to this set of 13,064 objects as the Luminosity Function (or LF) sample. All but 714 of these objects possess native SDSS magnitudes; the rest possess pseudo-SDSS magnitudes transformed from GSC observations.

The calibration region probes a sight line that passes directly through the mid-plane of the Milky Way, where the bulk of the dust in the Galaxy is thought to lie ( $h_{dust} \sim 125$  pc; Marshall et al. 2006). As the vast majority of the stars in our sample lie at distances in excess of 250 pcs, or two dust scale heights past the mid-plane of the Galaxy, we assume the bulk of the extinction along the line of sight to each star is foreground extinction. We therefore applied extinction corrections to the photometry for stars in our sample, using the extinction estimates measured by Schlegel et al. (1998) and stored in the SDSS database (for GSC detections, we adopt the reddening estimate of the nearest SDSS star in our sample). We use the relative extinctions in Table 6 of Schlegel et al. (1998) to apply corrections to our SDSS and 2MASS photometry using the  $R_V=3.1$  extinction laws of Cardelli et al. (1989) and O’Donnell (1994). These corrections are minimal, with a maximum  $E(i - J)$  of 0.11 mags and more than 95% of the sample possessing  $E(i - J) < 0.05$  mags; indeed, tests indicate that neglecting the effects of extinction produces a negligible impact on our results.

### 5.1. The SDSS/2MASS Color-Magnitude Relation For Late-Type Stars

Producing an LF from our photometric, magnitude-limited sample required us to estimate the absolute magnitude and distance of each star from its observed colors and an adopted color-magnitude relation (CMR). The CMR for low-mass stars is reasonably well known in the standard Johnsons-Cousins photometric system; the relative youth of the SDSS, however, make the transformation of standard CMRs onto the SDSS photometric system difficult for stars with red colors.

By spectroscopically classifying a sample of low-mass stars with measured SDSS and 2MASS colors, Hawley et al. (2002) derived photometric parallax relations for low-mass stars in SDSS by linking distinct color-spectral type and absolute magnitude-spectral type relations. Subsequent studies (West et al. 2005; Bochanski et al. 2007; West et al. 2008) have used larger samples to produce new measurements of the relation between spectral type and SDSS color, shifting the mean colors of a given spectral type somewhat bluer; these new

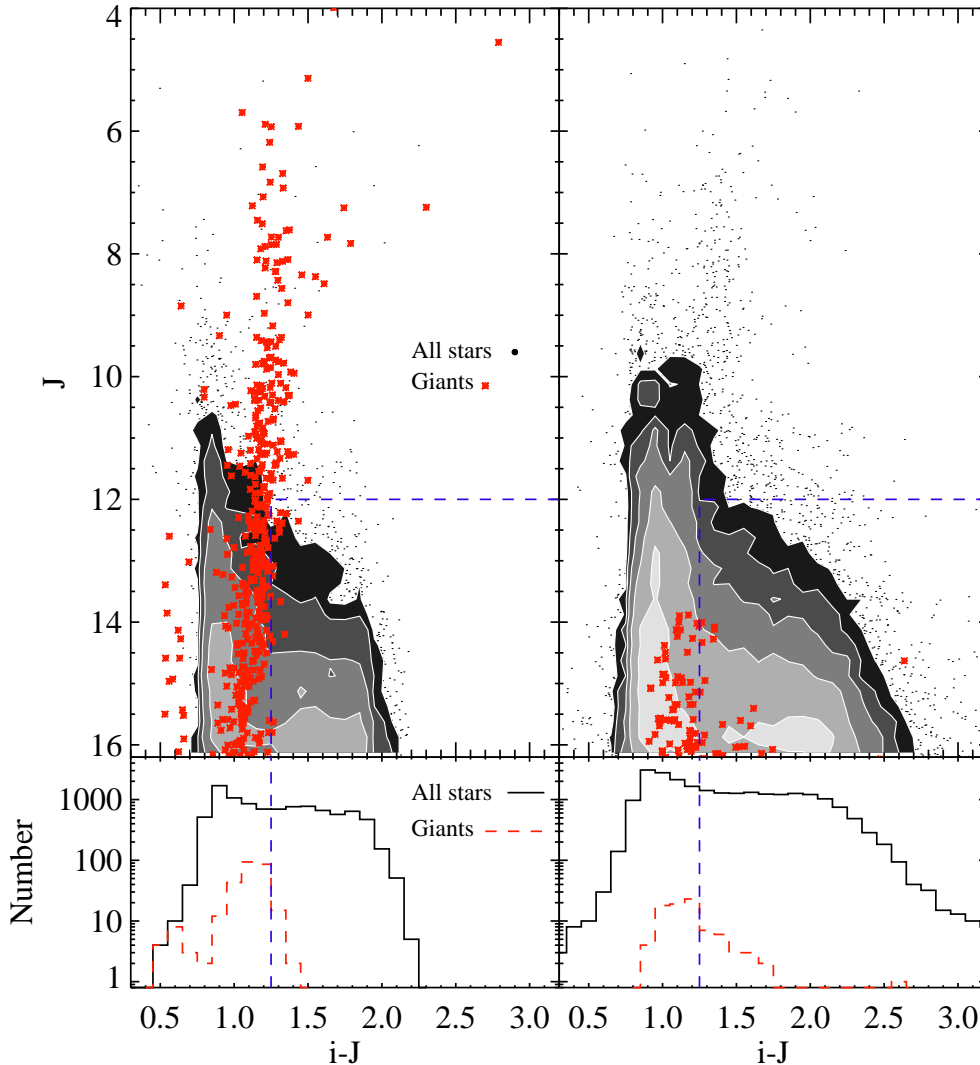


FIG. 8.— The location of giant star candidates in  $i - J$  vs.  $J$  color-magnitude space, as predicted by the standard TRILEGAL galaxy model (left panels) and as indicated by our photometric and spectroscopic catalogs (right panels). Dwarfs are shown as black points and contours in the top two panels, while giant stars are highlighted as red asterisks and identified using surface gravity in the TRILEGAL output or spectroscopic indices in the SDSS/2MASS sample. Dashed blue lines show photometric cuts of  $J > 12$  and  $i - J > 1.25$  ( $> K5$ ). Bottom panels comp are the  $i - J$  color distributions for all stars with  $J > 12$  (solid black line) and for giants (dashed red lines). To reduce contamination by giants, we restrict our luminosity function sample to sources with  $J > 12$  and  $i - J > 1.25$  (blue dashed lines).

color-spectral type relations produce new photometric parallax relations when coupled to the previously measured absolute magnitude-spectral type relation. Stellar colors and magnitudes in the SDSS and 2MASS systems have also been predicted using theoretical stellar models, such as those calculated by Girardi et al. (2002) and Dotter et al. (2007).

Ultimately, it would be best to determine the CMR by directly measuring native SDSS colors and magnitudes for stars with measured trigonometric parallaxes. In practice, nearly all such stars saturate the SDSS 2.5m camera, requiring observations with smaller telescopes to be transformed onto the 2.5m photometric system. Williams et al. (2002) and Golimowski et al. (2008) have observed parallax standards with the 0.6 meter SDSS Photometric Telescope (PT) and the USNO 1 meter telescope, using the relevant transformations (Tucker et al. 2006; Davenport et al. 2007) to place their photometry

on the SDSS 2.5 meter system. We fit preliminary photometric parallax relations to describe the dependence of  $M_J$  on  $r - J$  and  $i - J$  using 2MASS  $JHK$  magnitudes and transformed SDSS  $ugriz$  magnitudes kindly provided to us by Golimowski et al. (2008) prior to publication<sup>14</sup>. These empirical CMR fits are shown in Figure 9, along with SDSS/2MASS colors and magnitudes for individual stars measured in Appendix A.

The empirical CMR we have derived, however, suffers from some level of uncertainty. In particular, the data are too sparsely sampled to definitively reveal the presence or absence of a sharp break at  $i - J \sim 2.3$ , as is seen in other color-magnitude diagrams on the Johnson-Cousins system. As discussed by Reid & Gizis (1997),

<sup>14</sup> With an ultimate goal to measure the MF of low-mass stars, we chose to use CMRs to estimate  $M_J$ , for which well-established mass/luminosity relations exist (Henry & McCarthy 1993; Delfosse et al. 2000).

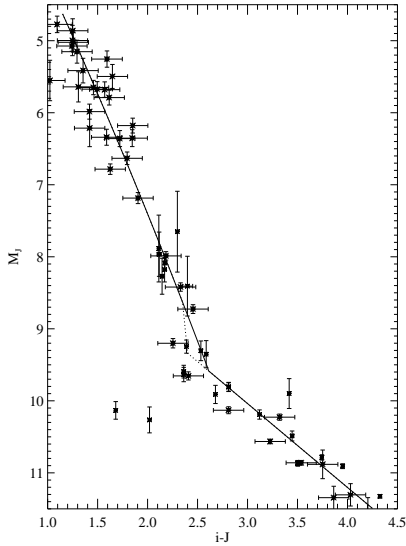


FIG. 9.— Color-magnitude relations necessary to estimate the distribution of stellar absolute magnitudes from the  $i - J$  colors of low-mass stars in the calibration region. The solid line shows a preliminary fit to the data of Golimowski et al. (2008), assuming a smooth fit through  $i - J \sim 2.3$ ; the dotted line shows a fit to the same data, but assuming the presence of a sharp break at  $i - J \sim 2.375$ . Shown for comparison (but not fitted directly) are the SDSS/2MASS colors and magnitudes of individual stars as reported in Appendix A.

this feature significantly affects the shape of the LF inferred from a magnitude limited photometric sample. In the absence of data clearly indicating the presence of a sharp break in the SDSS/2MASS CMR, for our analysis we adopt the smoothly varying CMR shown as a solid line in Fig. 9. Understanding the important role the CMR plays in measuring the luminosity and mass functions of magnitude limited samples, however, we include uncertainty in the empirical CMR as a potential source of systematic error in our analysis, which we discuss in more detail in §5.4.

### 5.2. The $V_{eff}$ Technique

Robust space density measurements of low-mass stars required a careful assessment of the volume we sampled for stars at each luminosity. In particular, we needed to account for the interplay between the vertical density gradient of the Galactic disk and the magnitude limits of our catalog. We did so by using the effective volume technique.

With roots in the  $\frac{V}{V_{max}}$  technique first introduced by Schmidt (1968), the concept of an ‘effective volume’ was first suggested by Huchra & Sargent (1973), who modified the  $\frac{V}{V_{max}}$  test to accommodate a spatial gradient as a function of position on the sky. Felten (1976) extended the  $V_{eff}$  formalism to include gradients as a function of depth along the line of sight and proved that the sum of  $\frac{1}{V_{eff}}$  for a sample of objects can serve as an unbiased estimator of their spatial density, even in situations where the objects are distributed inhomogeneously.

The effective volume of an object can be expressed mathematically as

$$V_{eff} = \Omega \int_{dmin}^{dmax} r^2 \frac{\rho}{\rho_0} dr \quad (6)$$

where  $\Omega$  is the observed solid angle,  $r$  is the position along the line of sight to an object,  $dmin$  is the minimum distance at which the object could be detected,  $dmax$  is the maximum distance at which the object could be detected, and  $\frac{\rho}{\rho_0}$  describes the ratio of the sampled density to the local density as a function of position along the line of sight. For non-uniform source distributions,  $\frac{\rho}{\rho_0}$  effectively weights each volume element along the line of sight according to the expected likelihood of finding a source in that volume, such that sampling equivalent effective volumes should result in samples with similar numbers of sources.

Using this methodology, space densities (represented by  $\Phi$ ) are given by the sum of  $\frac{1}{V_{eff}}$  for each source within the sample:

$$\Phi = \sum_N \frac{1}{V_{eff}} = \sum_N \frac{1}{\Omega \int_{dmin}^{dmax} r^2 \frac{\rho}{\rho_0} dr} \quad (7)$$

As shown by Huchra & Sargent (1973), the uncertainty in this estimator of  $\Phi$  is:

$$\sigma_{\Phi} = \sqrt{\sum_N \frac{1}{V_{eff}^2}} \quad (8)$$

Combining the bright and faint limits of our survey sample ( $J = 12$  and  $J = 16.2$  respectively) with the value of  $M_J$  estimated for a single source allows us to calculate its individual distance limits,  $dmin$  and  $dmax$ . Thus, all that remains in the calculation of  $V_{eff}$ , and thus  $\Phi(M_J)$ , is to integrate  $r^2 \frac{\rho}{\rho_0}$  between  $dmin$  and  $dmax$ .

### 5.3. Adopted Galactic Structure Model

Adopting a standard multi-component Galactic model allows us to calculate the stellar density profile expected along a given line of sight; the total density,  $\rho_{tot}$ , is simply the sum of the density profiles of the individual disk and halo components. Expressed as a function of position within the Galaxy (using the standard Galactic coordinates  $R$  and  $Z$ ), these profiles are:

$$\begin{aligned} \rho_{thin} &= \exp\left(-\frac{|Z|}{H_{thin}}\right) \exp\left(-\frac{|R|}{L_{thin}}\right) \\ \rho_{thick} &= \exp\left(-\frac{|Z|}{H_{thick}}\right) \exp\left(-\frac{|R|}{L_{thick}}\right) \\ \rho_{halo} &= \left(\sqrt{R^2 + \left(Z \times \frac{a}{c}\right)^2}\right)^{r_{halo}} \\ \rho_{tot} &= f_{thin} \frac{\rho_{thin}}{\rho_{thin,0}} + f_{thick} \frac{\rho_{thick}}{\rho_{thick,0}} + f_{halo} \frac{\rho_{halo}}{\rho_{halo,0}} \end{aligned}$$

The total stellar density at a given point in the Galaxy thus depends on the nine parameters given in Table 5. Given the Galactic latitude ( $b \sim -62$ ) and the color and magnitude limits of the calibration region sample,  $\frac{\rho}{\rho_0}$  is set primarily by the vertical profile of the thin disk; the thick disk only begins to dominate observed star counts at distances of  $\sim 1.25$  kpc, where even our most intrinsically luminous stars approach the faint limit of our sample.

In principle, the parameters in Table 5 can be constrained by fitting observed star counts to the output

TABLE 5  
GALACTIC STRUCTURE PARAMETERS

Parameter name	Parameter description	Adopted value
$f_{thin}$	thin disk stellar density in the solar neighborhood	$(1 - f_{thick} - f_{halo})$
$H_{thin}$	thin disk scale height	280 pc
$L_{thin}$	thin disk scale length	2500 pc
$f_{thick}$	thick disk stellar density in the solar neighborhood	5%
$H_{thick}$	thick disk scale height	900 pc
$L_{thick}$	thick disk scale length	3500 pc
$c/a$	halo flattening parameter axial ratio $c/a$	0.7
$r_{halo}$	exponent of halo power law density gradient	-2.75
$f_{halo}$	halo stellar density in the solar neighborhood	0.15%

of Galactic stellar population models produced with a range of Galactic structure parameters. The best estimates, however, are produced by comparing models to star counts along multiple lines of sight that sample regions of the Galaxy dominated by different Galactic components. Even in this best case, there often remain significant degeneracies between various Galactic structure parameters (e.g.,  $f_{thick}$  and  $H_{thick}$ ; see Fig. 1 of Siegel et al. 2002).

As the calibration region probes only a single sight line through the Galaxy, attempts to fit the Galactic model directly from the observed star counts produced unphysical results with significant degeneracies between parameters. A follow-up paper in this series (Bochanski et al. 2009, in prep.) will present robust Galactic structure parameters measured from low-mass stars detected across the entirety of the SDSS footprint; for now, however, we calculated  $\frac{\rho}{\rho_0}$  using standard Galactic structure parameters from the literature (see Table 1 of Siegel et al. 2002; Jurić et al. 2008) which are shown in Table 5. As Figure 10 demonstrates, the profile of stellar counts predicted by this model is in good agreement with the observed star counts in the calibration region over the entire magnitude range of our sample.

#### 5.4. The Luminosity Function of the Galactic Disk

Applying the  $V_{eff}$  technique to the LF sample, we obtained a first measure of the LF of the Galactic disk, shown in the top panel of Fig. 11 as green filled diamonds. Derived from a magnitude-limited sample of stars with distances up to a kiloparsec or more, this measurement suffers from Malmquist-type effects and represents the LF of *systems*, not individual stars, in the Galactic disk.

To account for the effects of unresolved binaries and Malmquist-like biases, we constructed an algorithm to reveal the intrinsic *stellar* LF required to reproduce the raw *system* LF measured from the calibration region sample. This routine uses a Monte Carlo approach to produce a simulated photometric sample given an input LF, CMR, and parameters to describe the adopted Galactic model and binary population. We then conduct a  $V_{eff}$  analysis on this synthetic sample, which incorporates both observational errors and the intrinsic width of the CMR. Using the difference between the synthetic ‘measured’ LFs and the actual raw LF measured from the calibration region to adjust the input LF used to run

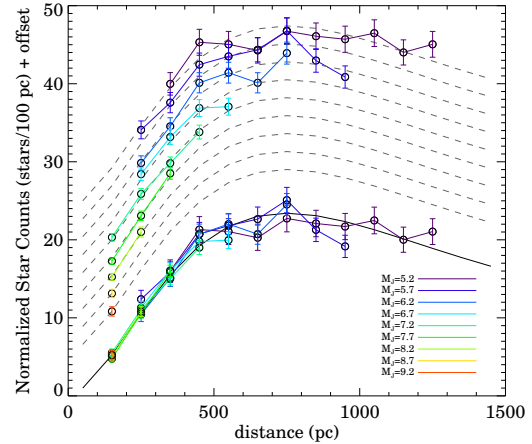


FIG. 10.— Star counts as a function of distance for stars with similar  $M_J$  values (colored circles). For clarity, each observed profile is shown twice: once compared to a common star count profile predicted for the Galactic structure parameters adopted here (solid black line, bottom), and once compared to the same model profile but with a unique vertical offset (dashed grey line). Observed star count profiles have been normalized such that the total number of stars along the line of sight matches the prediction of the model, allowing sets of stars with different local density normalizations to be compared to the same model profile. The Galactic structure model adopted here produces a good agreement between the observed and predicted star count profiles.

the next simulation, we iteratively converged on the true LF required to replicate our observed LF in the presence of these observational biases.

For our primary analysis, we adopted the fiducial Galactic model outlined in Table 5. We began by generating a synthetic set of star counts, randomly sampling the raw calibration region LF as an initial guess for the input LF and accounting for the increase in  $V_{eff}$  towards brighter  $M_J$ . We used the smooth empirical CMR shown as a solid line in Fig. 9 and the  $M_J$  vs. mass relation derived by Delfosse et al. (2000)<sup>15</sup> to assign masses and  $i - J$  colors to each star. We included an intrinsic dispersion in the CMR by sampling color offsets from a normal distribution with  $\sigma_{color} \sim 0.1$  mag, or equivalently, magnitude offsets with  $\sigma_{mag} \sim 0.5$  mag.

We accounted for the presence of unresolved binaries in our sample by randomly assigning secondary companions to synthetic stars with a mass dependent binary fraction,  $f_{bin}(M) = 0.45 - (0.7 - M_p)/4$ , consistent with observations of the stellar binary fraction in the Galactic disk (Duquennoy et al. 1991; Reid & Gizis 1997; Delfosse et al. 2004; Lada 2006; Burgasser et al. 2007). In our model, companion star luminosities were randomly selected from the same input LF used to generate the primary stars, but secondaries were required to have lower luminosities than their primaries. This quasi-independent sampling of the LF nicely reproduces the observed correlation between mass ratio and primary mass, producing a mass ratio distribution which peaks at 0.4 for stars more massive than  $0.6 M_\odot$  and at 0.9 for

<sup>15</sup> We note that the Delfosse et al. (2000)  $M_J$  vs. mass relations as published and archived on the A&A website and the arXiv preprint server contain typographical errors. The original authors confirm that the correct relation is  $\text{Log } \frac{M}{M_\odot} = (10^{-3} \times (1.6 + 6.01M_J + 14.888M_J^2 - 5.3557M_J^3 + 0.285181M_J^4))$ . (T. Forveille, priv. communication, 2008)

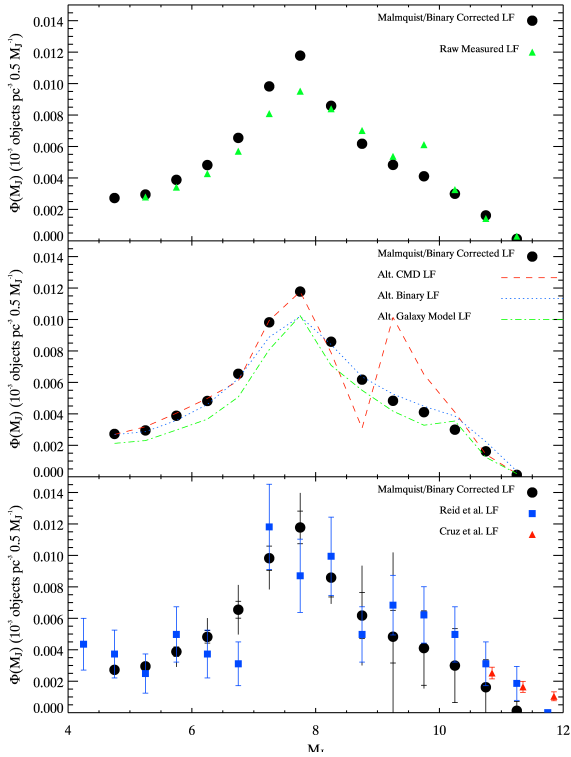


FIG. 11.— The calibration region luminosity function. *Top Panel:* System luminosity function measured from the calibration region (green triangles), and the resultant single-star luminosity function, after accounting for the impact of unresolved binaries and Malmquist type effects (black circles). *Middle Panel:* Systematic uncertainties in the luminosity function, shown by comparing the calibration region single-star luminosity function (black circles) with results obtained when adopting a color-magnitude relation with a sharp break at  $\sim M_4$  ( $i - J = 2.375$ ; red dashed line), a Galactic model with a  $\sim 20$  scale height (green dash-dot line), and correcting for binaries assuming a flat mass ratio distribution (blue dotted line). *Bottom Panel:* The calibration region single-star luminosity function (black circles), including error bars for statistical (hatted) and systematic (un-hatted) effects. Shown for comparison are luminosity functions derived from the volume complete 8 pc sample (blue filled squares; Reid et al. 2002) and for late-M/L dwarfs within 20 pc (red filled triangles; Cruz et al. 2007).

stars less massive than  $0.2 M_{\odot}$ .

We assumed that all binary systems in our sample are unresolved, based on the relatively poor spatial sampling of the 2MASS detectors ( $2''$  pixels). This assumption is not uniformly correct, as resolving a binary depends on the ratio of this resolution limit to the binary’s apparent separation, itself a function of both the physical separation of the companions and the distance to the system. Systems with an  $M_J = 8$  primary, for example, are resolved only if their separation exceeds 30-200 AU, depending on the location of the system within the volume to which we are sensitive to such stars; the situation is even worse for intrinsically brighter stars, which are drawn from a more distant volume and thus have smaller apparent separations for equivalent physical separations. As most binary stars have separations less than 100 AU, and our sample is dominated by stars at the largest distances, we treat all simulated binary systems as unresolved. Fluxes from each companion are merged to pro-

duce system magnitudes and colors, at which point random observational errors are added to produce a pseudo-observed photometric sample.

We then measured the LF of this sample using the same algorithm as applied to our observed sample, and used the difference between the two measured luminosity functions to modify the input LF used to produce the synthetic sample. After a small ( $n \sim 5$ ) number of iterations, the LF measured from the synthetic sample converges to that measured from the calibration region dataset. The final input LF whose ‘measured’ LF reproduces the raw calibration region LF is therefore a measure of the true LF of the calibration region after correcting for unresolved binaries and Malmquist-type biases, as each effect is included in producing the catalog of synthetic stars.

The calibration region LF with corrections for Malmquist biases and unresolved binaries is shown with black circles in each panel of Fig. 11. Somewhat counter-intuitively, aside from making the peak at  $M_J = 7$  more prominent, the corrected LF is very similar to the uncorrected LF we measure from the calibration region. Applying binary and Malmquist corrections independently showed that the two effects offset one another to a large degree; as discussed extensively by Stobie et al. (1989), the Malmquist correction shifts the peak of the LF to brighter magnitudes, primarily by decreasing the densities measured on the faint side of the LF peak. Accounting for unresolved binary systems, however, has the opposite effect – splitting binary systems into individual components increases the source density in the *stellar* LF above that of the *system* LF, and is most important for fainter stars, which are most likely to be hidden as secondaries to more luminous primaries. The primary impact of these corrections, therefore, is to increase the peak density of the LF (at  $M_J = 7.5$ ) by 20%; outside the  $7 < M_J < 8$  range, the *corrected stellar* LF is remarkably similar to the *measured system* LF.

To test how sensitive our LF measurement is to our underlying assumptions, we re-derived the LF after modifying the adopted CMR, Galactic model, and binarity prescription. We varied, in turn, the binary prescription to assign secondaries assuming a flat mass ratio distribution, the Galactic model by increasing the scale height of the thin disk by 50 parsecs, and the CMR by adopting the red dashed empirical fit in Fig. 9 that includes a sharp jump in magnitude at  $i - J = 2.375$ . The LFs derived under each of these modified assumptions are shown in the middle panel of Fig. 11.

We characterized the systematic uncertainties in our analysis as the fractional change induced in the LF by modifying each portion of the LF measurement algorithm; adding each of these individual uncertainties in quadrature produced a global estimate of the systematic uncertainties in our analysis, which is shown as an additional set of error bars for the corrected single-star LF in the bottom panel of Fig. 11. The binary correction introduces a relatively small  $\sim 5\%$  systematic uncertainty, rising above 10% only at the faintest magnitudes. The LF is somewhat more sensitive to the Galaxy model adopted in the  $V_{eff}$  analysis, typically producing a 20% uncertainty in the derived LF. The uncertainty in the LF due to the Galaxy model is more pronounced at brighter magnitudes, where the volume sampled is several scale heights above the plane of the Milky Way, and thus the

TABLE 6  
THE LUMINOSITY FUNCTION OF THE  
CALIBRATION REGION

$M_J$	Raw LF	Corrected LF	$\sigma_{\text{stat}}$	$\sigma_{\text{sys}}$
5.25	2.79	2.99	0.25	0.79
5.75	3.41	3.82	0.31	0.83
6.25	4.27	4.83	0.39	1.20
6.75	5.70	6.53	0.54	1.30
7.25	8.09	9.64	0.77	1.55
7.75	9.52	11.33	1.04	1.84
8.25	8.40	8.08	1.23	0.72
8.75	7.01	6.51	1.46	2.82
9.25	5.37	4.71	1.67	4.54
9.75	6.12	4.60	2.37	1.31
10.25	3.26	3.37	2.35	0.79
10.75	1.42	1.10	1.75	1.27
11.25	0.30	0.41	0.59	0.28

NOTE. — LFs and uncertainties reported in units of  $10^{-3}$  stars  $(0.5M_J)^{-1}pc^{-3}$

densities expected by the  $V_{\text{eff}}$  calculation are more sensitive to the adopted thin disk scale height.

The uncertainty in the exact behavior of the CMR at  $i - J \sim 2.375$ , however, introduces the largest systematic uncertainty into our analysis; LFs produced using the two empirical fits in Fig. 9 differ by more than 90% at  $M_J = 9.25$ . Reducing this uncertainty is clearly necessary to realize the full promise of the SDSS and 2MASS to characterize the low-mass stellar content of the Galactic disk. Doing so will require a concerted effort to transform photometry of trigonometric parallax standards from moderate aperture telescopes onto the native photometric system of the SDSS 2.5m.

The bottom panel of Figure 11 displays the single-star calibration region LF along with error bars accounting for both statistical and systematic effects. Shown for comparison are the low-mass stellar LFs measured by Reid et al. (2002) and Cruz et al. (2007) from volume complete samples in the solar neighborhood; with the exception of the  $M_J = 6.75$  bin, the calibration region LF agrees with the LFs measured from the volume complete samples, given the uncertainties in each measurement.

## 6. THE MASS FUNCTION

The same simulations that allowed us to correct our observed LF for unresolved binaries and Malmquist effects also provided an opportunity to measure the stellar mass function. Applying the  $V_{\text{eff}}$  technique to the synthetic stellar sample, but binning by mass instead of  $M_J$  magnitude, produced the MF shown in the top panel of Figure 12, again with both systematic and statistical error bars. The *logarithmically binned* mass function of the calibration region has a clear peak at  $M_* \sim 0.3 M_\odot$ . We note that the systematic error bars, due mainly to the uncertainty in the color magnitude relation, dominate the statistical error bars for all mass bins; until the SDSS/2MASS color-magnitude relation is clarified, we will be unable to reap the full benefit of a sample of this size.

We used a Markwardt minimization to fit various analytic forms to this data, with results shown in the top panel of Fig. 12. We fit a log normal form to the data, finding best fit values of  $A=0.1$  (in units of stars  $(\text{Log } M_\odot)^{-1}pc^{-3}$  for comparison with the values reported by

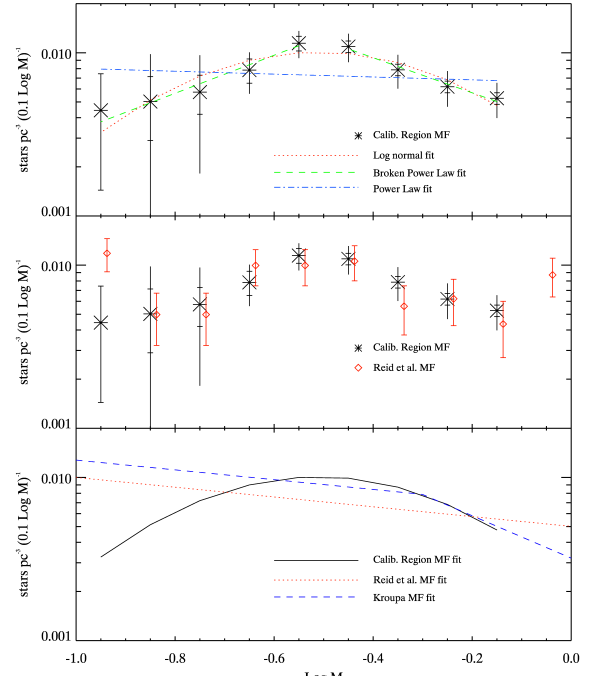


FIG. 12.— The *single-star* (not system) mass function ( $\frac{dN}{d\log M}$ ) of the Galactic disk as measured from the calibration region sample (aste risks; hatted error bars show statistical errors, unhatted error bars show systematic uncertainties). *Top Panel:* Analytic fits to the calibration region MF; log normal, power law, and broken power law fits to the data are shown as dotted, dot-dashed, and dashed lines respectively. An F-test indicates that the log normal fit provides the greatest fidelity given the number of parameters used to produce the fit. *Middle Panel:* A comparison between the calibration region MF and that derived by Reid et al. (2002) from the 8-pc volume complete sample (red diamonds); the two measurements agree within the uncertainties for all but the lowest mass point. *Bottom Panel:* Analytic descriptions of the *single-star* MFs presented by Reid et al. (2002) and Kroupa (2002), shown as red dotted and blue dashed lines respectively, compared to the log normal fit adopted here (solid black line). While the data underlying these fits agree well, the analytic descriptions diverge significantly, particularly at the low-mass end.

Chabrier 2003),  $M_c=0.29$ , and  $\sigma=0.32$ ; we also fit a single ( $\alpha = 1.1$ ) and broken power law ( $\alpha_{\log M > -0.5} = 2.04$ ;  $\alpha_{\log M < -0.5} = 0.2$ ) to the data as well. An F-test evaluates the quality of an analytic fit to a dataset relative to the number of degrees of freedom in the fit. Applying an F-test to these fits revealed that the log normal formalism produces a quantifiably better fit than a single power law: there is a less than 1% chance that the underlying distribution is truly a single power-law and that the improved quality of the log-normal fit is a random occurrence. A dual power law fit provides an even better fit than either the single power law or the log normal form, but at the cost of additional degrees of freedom; the F-test indicates there is a 35% chance that the dual power law fit does not provide a statistically superior fit to the data, and as such we adopted the log normal fit as the most efficient analytic description of our data.

$M_c$  represents the peak of the *logarithmically binned*

TABLE 7  
THE MASS FUNCTION OF THE  
CALIBRATION REGION

Log $M_*$	MF $\rho$	$\sigma_{\text{stat.}}$	$\sigma_{\text{sys.}}$
-0.15	5.42	0.44	1.29
-0.25	6.13	0.50	1.53
-0.35	7.91	0.65	1.52
-0.45	10.76	0.89	1.73
-0.55	10.82	1.18	1.54
-0.65	7.40	1.28	1.37
-0.75	6.07	1.59	3.54
-0.85	4.73	1.93	3.50
-0.95	5.61	3.38	1.47

NOTE. — MF densities and uncertainties are reported in units of  $10^{-3}$  stars  $(0.1 \log M_*)^{-1} \text{pc}^{-3}$ .

mass function, such that while the density of stars per logarithmic mass bin declines for masses less than  $M_c$ , the width of each bin in *linear* mass units is also changing as well. As a result, a log normal MF with a given  $M_c$  corresponds to a *linearly binned* MF whose peak occurs at smaller masses than  $M_c$ . The log normal fit described above corresponds to a *linearly binned* MF that turns over at  $0.17 M_\odot$ .

The MF we measure here agrees well with previous investigations. Using a Monte Carlo routine to refit the MF after applying random offsets consistent with each datapoint’s total error budget, we derive 90% confidence intervals for the log-normal fits’ parameters of  $A=0.08\text{--}0.12$ ,  $M_c=0.20\text{--}0.50$ , and  $\sigma=0.22\text{--}0.37$ . These agree well with the values reported by Chabrier (2005), with the exception of  $\sigma$ , for which Chabrier finds a somewhat larger value of 0.55, outside the bounds of our 90% confidence interval. This may result from the difference in the range of masses studied here and by Chabrier; Chabrier’s work attempts to describe the MF well above and below the masses sampled here, which may drive the fit to larger values of  $\sigma$ , and wider MF peaks. We also include in the middle panel of Fig. 12 the individual datapoints for the MF constructed by Reid et al. (2002), which agree within  $1 \sigma$  with the datapoints reported here for all but the lowest mass bin. Similarly, the  $\alpha = 1.1$  power law fit to the entire mass range sampled here is a good match to the  $\alpha=1.2$  power law measured by Reid et al. (2002).

Simply comparing analytic fits from other studies to the MF data measured here, however, can give the potentially false impression of disagreement in the underlying MFs. This is due in part to the sensitivity of analytic fits to the exact formalism chosen to represent the data, as well the exact range of masses spanned by the fit. As shown in the bottom panel of Fig. 12, the log normal description of the MF data reported here diverges strongly from the analytic fits reported by Reid et al. (2002) and Kroupa (2002), which would seem to provide evidence for significant MF differences. In particular, the log normal fit presented here predicts an MF that peaks in the stellar regime, while the break points adopted for the power-law fits measured by Reid et al. (2002) and Kroupa (2002) imply that the MF rises all the way to the sub-stellar limit. As shown previously, however, the individual MF datapoints derived here and by Reid et al. (2002) agree well, revealing that these variations are due more to differences in the formalisms adopted to describe the MF

than to confident detections of significant MF differences.

Traditionally, the utility of analytic descriptions of the data has been to produce a more robust description of a potentially noisy dataset, collapsing the many degrees of freedom of the sample to improve the quality of the measurement of a reduced set of parameters. Given the richness of modern-day astronomical datasets, however, where one can construct samples of stellar populations that contain thousands, and in some cases millions, of objects useful for deriving mass functions, the underlying data can produce MFs with vanishingly small statistical error bars, and systematic errors are not reduced by describing the data with analytic fits. As a result, we are entering the regime where we create more noise than signal by comparing analytic descriptions of the MF, which impose structure on the data *a priori*, rather than comparing actual MF datapoints with statistical and systematic error bars.

Having validated this method to generate a low-mass luminosity function from matched SDSS/2MASS datasets, future studies (Bochanski et al., in prep.) will extend this technique to the entirety of the SDSS footprint, producing simultaneous measurements of the low-mass MF and Galactic structure parameters of the thin and thick disks.

## 7. CONCLUSIONS

1. We have identified a sample of more than 13,000 candidate low-mass stars detected within 30 square degrees of 2MASS, SDSS and/or GSC imaging. Empirical tests verify the sample is more than 99% complete to  $J = 16.2$ , and more than 90% complete at even the reddest colors.
2. Analysis of the spectroscopic sample reveals that exotic contaminants, such as QSOs, extragalactic stellar populations, CVs, and white dwarf/M dwarf pairs, comprise less than 0.3% of our matched sample.
3. Photometric  $i-J$  color provides a reliable proxy for stellar spectral type and  $T_{\text{eff}}$ ; we measure dispersions of 1 subclass for a given 0.1 magnitude slice in  $i-J$ , or of 0.1 magnitude in  $i-J$  for objects with a given MK spectral type.
4. In a small percentage of cases (20/9624; 0.02%), a star’s observed spectral type differs significantly from that expected on the basis of its photometric  $i-J$  color. This usually occurs when the 2MASS and SDSS detections of a close visual binary are improperly matched, and we have identified an  $i-z$  vs.  $i-J$  color cut which can be used to eliminate such spurious detections from the sample.
5. Analysis of the kinematic and spectroscopic properties of our sample reveal 88 candidate subdwarfs, representing a subdwarf fraction of 0.68% for our broader sample. As the bulk of the candidate subdwarfs (69/88) were identified kinematically, and proper motion catalogs are biased towards objects with large space motions such as subdwarfs, this is an upper limit to the true subdwarf fraction of our photometric sample.

6. TRILEGAL simulations of the Galactic stellar population predict giant stars will contaminate our sample at the 4% level globally, but with giants exceeding 10% of stars with  $i - J \sim 1.15$ . Candidate giant stars identified in our sample using spectral indices verify the colors of giants predicted by the TRILEGAL simulation. Restricting our analysis to sources with  $J > 12$  and  $i - J > 1.25$ , however, reduce contamination of our sample by giant stars to a manageable level (less than 2% in the bluest, most contaminated color bin) while sacrificing only a handful of bona fide low-mass dwarf stars.
7. After correcting for unresolved binaries and Malmquist effects, we find the luminosity function of the Galactic disk is consistent with that measured from volume complete samples of the solar neighborhood. The dominant systematic uncertainty in our analysis is due to the remaining uncertainty in the SDSS/2MASS CMR, which translates into a 70% uncertainty at the peak of the stellar LF. Systematic effects due to the binary correction prescription and the adopted Galactic model are comparatively small, at the 10-20% level.
8. The logarithmically binned mass function measured from our sample peaks at  $0.3 M_{\odot}$  and agrees within  $1\sigma$  for all but one data point of the mass function measured by Reid et al. (2002) from their volume complete sample. A log normal characterization with  $A=0.1$  (in units of stars  $(\text{Log } M_{\odot})^{-1} pc^{-3}$  for comparison with the values reported by Chabrier 2003),  $M_c=0.29$ , and  $\sigma=0.32$  provides an adequate description of the data, with 90% confidence intervals for each parameter of  $A=0.08-0.12$ ,  $M_c=0.20-0.50$ , and  $\sigma=0.22-0.37$ . These 90% confidence intervals correspond to *linearly binned* mass functions peaking between  $0.27 M_{\odot}$  and  $0.12 M_{\odot}$ , where the best fit MF turns over at  $0.17 M_{\odot}$ . A power law fit to the entire mass range sampled here, however, returns a best fit of  $\alpha=1.1$  (where the Salpeter slope is  $\alpha = 2.35$ ); a broken power law returns  $\alpha=2.04$  at masses greater than  $\log M = -0.5$  ( $M=0.32 M_{\odot}$ ), and  $\alpha=0.2$  at lower masses.
9. We emphasize that comparisons of analytic MF fits, rather than the underlying data, can give the false impression of MF variations even when the underlying data agree well. We are entering the regime where we create more noise than signal by comparing analytic descriptions of the MF, which impose structure on the data *a priori*, rather than comparing the actual MF datapoints themselves.

We thank Michael Meyer and Charles Lada for helping clarify the current empirical constraints on the fraction and properties of low-mass multiple systems, August Muench and Thomas Greene for useful discussions of the mass function of low-mass stars in young clusters and the effects of extinction, and Chris McKee for a careful and thoughtful reading of a previous draft of this paper. We also owe a debt of gratitude to Connie

Rockosi for assistance in obtaining and analyzing SDSS data on occasions too numerous to count, and to Russet, Jack, Bill and John, the APO observing specialists whose assistance, patience, and occasional skirting of the telescope's strict wind limit were instrumental in helping obtain the complete spectroscopic sample necessary for this work. We also thank the anonymous referee, whose comments have improved this manuscript, resulting in a clearer, more concise presentation of this work.

Funding for the SDSS and SDSS-II has been provided by the Alfred P. Sloan Foundation, the Participating Institutions, the National Science Foundation, the U.S. Department of Energy, the National Aeronautics and Space Administration, the Japanese Monbukagakusho, the Max Planck Society, and the Higher Education Funding Council for England. The SDSS Web Site is <http://www.sdss.org/>.

The SDSS is managed by the Astrophysical Research Consortium for the Participating Institutions. The Participating Institutions are the American Museum of Natural History, Astrophysical Institute Potsdam, University of Basel, University of Cambridge, Case Western Reserve University, University of Chicago, Drexel University, Fermilab, the Institute for Advanced Study, the Japan Participation Group, Johns Hopkins University, the Joint Institute for Nuclear Astrophysics, the Kavli Institute for Particle Astrophysics and Cosmology, the Korean Scientist Group, the Chinese Academy of Sciences (LAMOST), Los Alamos National Laboratory, the Max-Planck-Institute for Astronomy (MPIA), the Max-Planck-Institute for Astrophysics (MPA), New Mexico State University, Ohio State University, University of Pittsburgh, University of Portsmouth, Princeton University, the United States Naval Observatory, and the University of Washington.

The Two Micron All Sky Survey was a joint project of the University of Massachusetts and the Infrared Processing and Analysis Center (California Institute of Technology). The University of Massachusetts was responsible for the overall management of the project, the observing facilities and the data acquisition. The Infrared Processing and Analysis Center was responsible for data processing, data distribution and data archiving.

This research has made use of NASA's Astrophysics Data System Bibliographic Services, the SIMBAD database, operated at CDS, Strasbourg, France, and the VizieR database of astronomical catalogues (?). K.R.C gratefully acknowledges the support of NASA grant 80-0273 during the completion of this work. Support for this work was provided by NASA through the Spitzer Space Telescope Fellowship Program.

#### A1. APPENDIX: PHOTOMETRY OF PARALLAX STANDARDS ON THE SDSS SYSTEM

An accurate characterization of the color-magnitude diagram for low-mass stars is of critical importance for inferring stellar densities and distributions from purely photometric datasets. By mining the SDSS database, and conducting supplementary observations with the NMSU 1m telescope, we have obtained colors and magnitudes on the SDSS photometric system for 76 stars and brown dwarfs with measured trigonometric parallaxes.

##### A1.1. Mining the SDSS database for Parallax Standards

As the SDSS contains photometry of nearly a quarter of the night sky, thousands of stars with measured trigonometric standards lie within the survey footprint. While the vast majority of parallax standards are so bright that they saturate SDSS imaging, parallax standards with servicable SDSS observations represent a valuable opportunity to map the main sequence color-magnitude relation directly from SDSS photometry, obviating the need to employ delicate, color-dependent transformations to place observations from other telescopes onto the SDSS photometric system.

To identify a catalog of parallax standards with native SDSS photometry, we have searched the SDSS database for detections of objects contained within several publicly available parallax catalogs (Monet et al. 1992; van Altena et al. 1995; Tinney et al. 1995; Perryman et al. 1997; Dahn et al. 2002; Gould & Chanamé 2004; Vrba et al. 2004). Culling the list to remove objects with flags indicative of severe photometric problems (ie, SATURATED-CENTER and/or INTERP-CENTER) left 40 objects with native SDSS photometry and direct trigonometric parallax measurements. SDSS and 2MASS photometry for these objects, as well as their measured trigonometric parallaxes, are presented in Table 8. Figure 9 displays the locations of these sources in an  $i - J$  vs.  $M_J$  color-magnitude diagram.

#### A1.2. Observations of Parallax Standards with the NMSU 1m

Additional constraints on the location of the lower main sequence in SDSS/2MASS color-magnitude space can be derived by transforming observations from secondary telescopes onto the native SDSS photometric system. Using time on the NMSU 1m telescope made available to the public through the NSF PREST program, we obtained  $r'i'z'$  observations of 36 stars with mea-

sured trigonometric parallaxes, along with ‘deep’ observations of fields containing late type stars with unsaturated SDSS photometry.

The NMSU 1m telescope features a 2048x2048 E2V CCD providing a plate scale of 0.467 arcsec/pixel. Observations were carried out in robotic mode under good conditions (clear to light cirrus, seeing 1-2'') on February 6th and 7th, 2007. Images were bias subtracted, flat fielded, and overscan corrected before instrumental magnitudes were measured via aperture photometry, using apertures with a 15 pixel radius and sky annuli 15 pixels in width with an inner radius of 25 pixels. Observations of  $u'g'r'i'z'$  photometric standards Smith et al. (2002) demonstrate internal photometric accuracy of  $\sigma=0.04$  magnitudes.

Comparing instrumental magnitudes to SDSS database magnitudes for stars in the ‘deep’ SDSS fields allow the derivation of airmass corrections simultaneously with the zeropoints and color-terms required to transform from NMSU instrumental magnitudes onto the SDSS photometric system. The accuracy of the NMSU to SDSS transformation is limited by statistical uncertainties in NMSU detections of stars in the ‘deep’ SDSS fields; residuals in the transformed SDSS  $i$  magnitudes range from 0.03 to 0.13 magnitudes for sources with  $i = 15 - 18$ , respectively. Similar results are seen for stellar colors, with maximum  $r - i$  and  $i - z$  residuals at the faint ( $i = 18$ ) end of 0.15 and 0.2 magnitudes, respectively. As a result, we adopt conservative uncertainties for our transformed SDSS photometry of 0.15 magnitudes in  $i$  and  $r - i$ , and 0.2 magnitudes in  $i - z$ .

The SDSS magnitudes we derive for these sources from our transformed NMSU photometry are presented in Table 9, along with their 2MASS magnitudes and measured trigonometric parallaxes. These sources are also shown in Fig. 9.

#### REFERENCES

- Abazajian, K. et al. 2004, AJ, 128, 502  
 Adelman-McCarthy, J. K. et al. 2008, ApJS, 175, 297  
 —. 2006, ApJS, 162, 38  
 Bagnulo, S., Jehin, E., Ledoux, C., Cabanac, R., Melo, C., Gilmozzi, R., & The ESO Paranal Science Operations Team. 2003, The Messenger, 114, 10  
 Bessell, M. S., & Brett, J. M. 1988, PASP, 100, 1134  
 Bessell, M. S., & Wickramasinghe, D. T. 1979, ApJ, 227, 232  
 Bochanski, J. J., West, A. A., Hawley, S. L., & Covey, K. R. 2007, AJ, 133, 531  
 Burgasser, A. J., et al. 2007, in Protostars and Planets V, ed. B. Reipurth, D. Jewitt, & K. Keil, 427–441  
 Cardelli, J. A., Clayton, G. C., & Mathis, J. S. 1989, ApJ, 345, 245  
 Chabrier, G. 2003, PASP, 115, 763  
 Chabrier, G. 2005, in Astrophysics and Space Science Library, Vol. 327, The Initial Mass Function 50 Years Later, ed. E. Corbelli, F. Palla, & H. Zinnecker, 41–+  
 Corbelli, E., Palla, F., & Zinnecker, H., eds. 2005, Astrophysics and Space Science Library, Vol. 327, The Initial Mass Function 50 years later  
 Covey, K. R. 2006, PhD thesis, University of Washington, United States – Washington  
 Covey, K. R. et al. 2007, AJ, 134, 2398  
 Cruz, K. L. et al. 2007, AJ, 133, 439  
 Cutri, R. M. et al. 2003, VizieR Online Data Catalog, 2246, 0  
 Cutri, R. M., et al. 2007, Explanatory Supplement to the 2MASS All Sky Data Release and Extended Mission Products  
 Dahn, C. C. et al. 2002, AJ, 124, 1170  
 Danks, A. C., & Dennefeld, M. 1994, PASP, 106, 382  
 Davenport, J. R. A., Bochanski, J. J., Covey, K. R., Hawley, S. L., West, A. A., & Schneider, D. P. 2007, AJ, 134, 2430  
 Delfosse, X. et al. 2004, in ASP Conf. Ser. 318: Spectroscopically and Spatially Resolving the Components of the Close Binary Stars, 166–174  
 Delfosse, X., Forveille, T., Ségransan, D., Beuzit, J.-L., Udry, S., Perrier, C., & Mayor, M. 2000, A&A, 364, 217  
 Dotter, A., Chaboyer, B., Jevremović, D., Baron, E., Ferguson, J. W., Sarajedini, A., & Anderson, J. 2007, AJ, 134, 376  
 Duquenois, A., Mayor, M., & Halbwachs, J.-L. 1991, A&AS, 88, 281  
 Felten, J. E. 1976, ApJ, 207, 700  
 Fluks, M. A., Plez, B., The, P. S., de Winter, D., Westerlund, B. E., & Steenman, H. C. 1994, A&AS, 105, 311  
 Fukugita, M., Ichikawa, T., Gunn, J. E., Doi, M., Shimasaku, K., & Schneider, D. P. 1996, AJ, 111, 1748  
 Girardi, L., Bertelli, G., Bressan, A., Chiosi, C., Groenewegen, M. A. T., Marigo, P., Salasnich, B., & Weiss, A. 2002, A&A, 391, 195  
 Girardi, L., Groenewegen, M. A. T., Hatziminaoglou, E., & da Costa, L. 2005, A&A, 436, 895  
 Gizis, J. E. 1997, AJ, 113, 806  
 Golimowski, D. A., Henry, T. J., Reid, I. N., & Uomoto, A. 2008, SDSS parallaxes (in prep.)  
 Gould, A., & Chanamé, J. 2004, ApJS, 150, 455  
 Gunn, J. E. et al. 1998, AJ, 116, 3040  
 —. 2006, AJ, 131, 2332  
 Hawley, S. L. et al. 2002, AJ, 123, 3409  
 Henry, T. J., & McCarthy, D. W. 1993, AJ, 106, 773

TABLE 8  
NATIVE SDSS PHOTOMETRY OF PARALLAX STANDARDS

Star Name	SDSS $i$	SDSS $r-i$	SDSS $i-z$	2MASS $J$	2MASS $J-H$	2MASS $H-K_s$	$\pi$ (mas/yr)	$\pi$ err.	$\pi$ ref.
LHS 1970	16.26	0.83	0.49	14.58	0.58	0.12	12.9	0.7	1
G 195-022	12.79	1.74	1.00	10.26	0.56	0.30	64.4	4.0	1
LHS 2364	17.01	0.29	0.16	15.98	0.45	-0.03	38.3	2.7	1
LP 323-239	13.55	1.66	0.90	11.18	0.44	0.26	48.1	1.9	1
LHS 2828	14.81	2.23	1.14	12.00	0.52	0.33	36.5	0.9	1
LHS 2930	14.29	2.82	1.52	10.79	0.65	0.35	103.8	1.3	1
LHS 3061	17.54	1.20	0.60	15.52	0.51	0.11	8.9	0.7	1
J090551.11+553218.5	13.66	1.39	0.78	11.49	0.60	0.23	20.9	0.97	2
J091841.52+582747.5	14.33	1.44	0.74	12.16	0.58	0.28	16.0	1.2	2
J103327.6+472202.6	14.01	1.51	0.83	11.71	0.65	0.26	15.4	4.0	2
J113212.96+003632.5	14.18	1.44	0.95	11.78	0.52	0.29	21.2	4.0	2
J113304.07+131816.9	14.91	1.36	0.69	12.79	0.61	0.27	10.8	1.5	2
J120723.99+130213.9	15.68	2.01	1.05	13.00	0.60	0.32	24.1	1.4	2
J123426.4+391309.4	14.21	1.36	0.76	12.10	0.57	0.24	14.4	3.1	2
J132820.87+300319	16.73	2.50	1.37	13.31	0.67	0.35	20.7	2.0	2
J135921.6+251403.1	15.02	1.89	1.00	12.43	0.56	0.31	24.2	2.1	2
J141436.71+160121.7	14.39	1.73	0.90	12.00	0.59	0.31	28.1	1.1	2
J155719.67+074500.1	14.90	1.44	0.75	12.76	0.52	0.27	12.7	1.5	2
LP374-4	17.01	0.29	0.16	15.98	0.45	-0.03	38.3	2.8	3
LP130-226	15.32	2.54	1.28	12.20	0.51	0.33	39.6	1.1	3
LP323-239	13.55	1.66	0.90	11.18	0.44	0.26	49.0	2.2	3
LP499-5	14.81	2.23	1.14	12.00	0.52	0.33	36.5	1.0	3
LP98-79	14.29	2.82	1.52	10.79	0.65	0.35	10.38	1.4	3
J003259.36+141036.4	23.09	1.16	3.69	16.83	1.18	0.70	30.1	5.2	4
J010752.46+004156.3	21.19	2.02	2.55	15.82	1.31	0.80	64.1	4.5	4
J015141.68+124429.4	22.85	1.60	3.39	16.57	0.96	0.42	46.7	3.4	4
TVLM 832-10443	17.08	2.86	1.67	13.13	0.69	0.48	36.0	0.4	5
J074642.48+200031.6	16.08	2.57	1.85	11.76	0.75	0.54	81.9	0.3	5
J082519.44+211550.3	20.61	2.80	2.76	15.10	1.31	0.76	93.8	1.0	5
J083008.16+482847.2	21.22	2.35	3.14	15.44	1.10	0.67	76.4	3.4	4
TVLM 213-2005	17.14	2.77	1.66	13.39	0.65	0.48	30.1	0.4	5
LHS 2471	14.70	2.60	1.50	11.26	0.60	0.40	70.2	2.1	5
J125453.99-012247.4	22.25	2.05	4.22	14.89	0.80	0.25	75.7	2.9	4
LHS 2924	16.19	2.39	1.80	11.99	0.76	0.48	95.0	5.7	5
LHS 2930	14.29	2.82	1.52	10.79	0.65	0.35	103.3	1.3	5
J143517.28-004612.8	20.35	2.58	1.79	16.48	0.87	0.29	9.9	5.2	4
J144600.48+002451.9	20.75	2.68	2.18	15.89	1.38	0.58	45.5	3.3	4
TVLM 513-46546	16.08	2.64	1.79	11.87	0.69	0.47	94.4	0.6	5
J171145.59+223204.2	22.15	1.38	2.33	17.09	1.29	1.07	33.1	4.8	4
J225529.03-003434	19.85	2.36	1.91	15.65	0.89	0.32	16.2	2.6	4

NOTE. — Reference 1: van Altena et al. (1995)  
Reference 2: Gould & Chanamé (2004)  
Reference 3: Monet et al. (1992)  
Reference 4: Vrba et al. (2004)  
Reference 5: Dahn et al. (2002)

Hogg, D. W., Finkbeiner, D. P., Schlegel, D. J., & Gunn, J. E. 2001, *AJ*, 122, 2129  
Huchra, J., & Sargent, W. L. W. 1973, *ApJ*, 186, 433  
Ivezić, Ž. et al. 2002, in *ASP Conf. Ser. 284: AGN Surveys*, 137–+  
Ivezić, Ž. et al. 2004, *Astronomische Nachrichten*, 325, 583  
Jurić, M. et al. 2008, *ApJ*, 673, 864  
Klessen, R. S., Burkert, A., & Bate, M. R. 1998, *ApJ*, 501, L205+  
—. 2002, *Science*, 295, 82  
Lada, C. J. 2006, *ApJ*, 640L, 63  
Lançon, A., & Wood, P. R. 2000, *A&AS*, 146, 217  
—. 1992, *MNRAS*, 256, 641  
Le Borgne, J.-F., et al. 2003, *A&A*, 402, 433  
Luhman, K. L. 2004, *ApJ*, 617, 1216  
Lupton, R., Gunn, J. E., Ivezić, Z., Knapp, G. R., Kent, S., & Yasuda, N. 2001, in *ASP Conf. Ser. 238: Astronomical Data Analysis Software and Systems X*, 269–+  
Lupton, R. H., Gunn, J. E., & Szalay, A. S. 1999, *AJ*, 118, 1406

Malyuto, V., Oestreicher, M. O., & Schmidt-Kaler, T. 1997, *MNRAS*, 286, 500  
Malyuto, V., & Schmidt-Kaler, T. 1999, *Astronomische Nachrichten*, 320, 71  
Marshall, D. J., Robin, A. C., Reylé, C., Schultheis, M., Picaud, S. 2006, *A&A*, 453, 635  
Miller, G. E., & Scalo, J. M. 1979, *ApJS*, 41, 513  
Monet, D. G., Dahn, C. C., Vrba, F. J., Harris, H. C., Pier, J. R., Luginbuhl, C. B., & Ables, H. D. 1992, *AJ*, 103, 638  
Morell, O. 1988, in *IAU Symp. 132: The Impact of Very High S/N Spectroscopy on Stellar Physics*, ed. G. Cayrel de Strobel & M. Spite, 519–+  
Morrison, H. L. et al. 2003, *AJ*, 125, 2502  
Munn, J. A. et al. 2004, *AJ*, 127, 3034  
O'Donnell, J. E. 1994, *ApJ*, 422, 158  
Padoan, P., & Nordlund, Å. 2002, *ApJ*, 576, 870  
Perryman, M. A. C. et al. 1997, *A&A*, 323, L49

TABLE 9  
NMSU-1M PHOTOMETRY OF PARALLAX STANDARDS

Star Name	SDSS $i$	SDSS $r-i$	SDSS $i-z$	2MASS $J$	2MASS $J-H$	2MASS $H-K_s$	$\pi$ (mas/yr)	$\pi$ err.	$\pi$ ref.
AC +61 23399	9.72	0.66	0.32	8.150	0.69	0.14	32.1	1.6	1
BD+37 2337	9.29	0.29	0.12	8.033	0.56	0.11	24.99	1.6	1
CN Leo	10.41	2.39	1.38	7.085	0.60	0.40	425.0	7.0	2
G 88-28	9.66	0.96	0.48	7.818	0.64	0.23	50.9	2.7	1
G 96-1	9.67	0.16	0.01	8.645	0.46	0.02	24.07	3.1	1
G 176-8	9.76	0.76	0.41	8.107	0.67	0.22	30.1	2.3	1
G 198-37	9.23	0.69	0.33	7.610	0.64	0.20	43.25	2.0	1
G 199-13	9.09	0.22	0.06	8.000	0.50	0.10	22.7	1.2	1
G 221-23	8.37	0.47	0.20	6.873	0.61	0.15	57.53	2.7	1
G 221-24	9.23	0.95	0.45	7.379	0.58	0.23	57.53	2.7	1
G 222-1	9.55	0.71	0.30	7.955	0.72	0.14	28.8	1.4	1
G 250-34	9.67	0.94	0.46	7.872	0.61	0.24	56.51	2.2	1
G 256-10	10.28	0.33	0.07	9.131	0.48	0.13	27.00	10.0	2
GJ 3452	9.68	1.07	0.54	7.772	0.55	0.27	76.3	2.6	1
GJ 3504	15.26	2.48	1.40	12.035	0.56	0.34	50.8	0.5	2
GJ 3855	14.33	2.74	1.50	10.79	0.65	0.35	103.3	1.3	2
GJ 585.1	9.15	0.53	0.23	7.693	0.61	0.18	39.0	1.7	1
GJ 9455B	10.01	0.19	0.04	8.948	0.38	0.13	20.7	10.6	1
GSC 03722-00302	9.70	0.30	0.09	8.450	0.51	0.12	20.39	2.0	1
HD 24916	7.31	0.34	0.12	6.063	0.58	0.15	63.41	2.0	1
HD 284552	9.78	0.38	0.14	8.427	0.59	0.15	24.98	2.0	1
HIC 33805	9.72	0.64	0.32	8.129	0.59	0.19	43.9	2.2	1
LHS 35	10.68	1.59	0.80	8.424	0.50	0.27	143.0	4.0	2
LHS 197	14.37	2.26	1.14	11.559	0.50	0.29	51.8	1.0	2
LHS 224	10.99	1.75	0.91	8.537	0.44	0.32	109.1	2.8	2
LHS 231	14.01	1.78	0.90	11.606	0.49	0.24	40.7	1.0	2
LHS 287	10.82	1.57	0.83	8.493	0.49	0.29	96.7	2.3	2
LHS 303	9.72	0.87	0.46	7.994	0.60	0.23	47.1	2.4	1
LHS 331	12.17	1.48	0.74	9.983	0.48	0.28	39.9	1.0	2
LHS 2914	12.04	0.29	0.13	10.803	0.47	0.16	27.0	13.0	2
LHS 1653	10.35	0.45	0.22	8.926	0.61	0.13	28.7	3.4	1
LTT 13340	9.29	0.32	0.15	8.036	0.53	0.12	23.2	1.8	1
NLTT 36978	9.58	0.31	0.12	8.287	0.55	0.09	23.6	1.7	1
NSV 5426	10.14	0.35	0.15	8.835	0.55	0.15	23.0	2.2	1
NSV 6424	9.45	0.51	0.24	8.031	0.70	0.13	39.0	1.8	1
TVLM 263-71765	17.11	2.70	1.71	13.363	0.64	0.41	31.9	2.9	3

NOTE. — Reference 1: Perryman et al. (1997)  
Reference 2: van Altena et al. (1995)  
Reference 3: Tinney et al. (1995)

- Pier, J. R., Munn, J. A., Hindsley, R. B., Hennessy, G. S., Kent, S. M., Lupton, R. H., & Ivezić, Z. 2003, *AJ*, 125, 1559
- Prugniel, P., & Soubiran, C. 2001, *A&A*, 369, 1048
- Reid, I. N., & Gizis, J. E. 1997, *AJ*, 113, 2246
- Reid, I. N., Brewer, C., Brucato, R. J., McKinley, W. R., Maury, A., Mendenhall, D., Mould, J. R., Mueller, J., Neugebauer, G., Phinney, J., Sargent, W. L. W., Schombert, J., Thicksten, R. 1991, *PASP*, 103, 661
- Reid, I. N., Gizis, J. E., & Hawley, S. L. 2002, *AJ*, 124, 2721
- Reid, I. N., Hawley, S. L., & Gizis, J. E. 1995, *AJ*, 110, 1838
- Reid, N., & Hawley, S. L. 2000, *New light on dark stars: red dwarfs, low mass stars, brown dwarfs* (Springer)
- Reipurth, B., & Clarke, C. 2001, *AJ*, 122, 432
- Salpeter, E. E. 1955, *ApJ*, 121, 161
- Scalo, J. M. 1986, *Fundamentals of Cosmic Physics*, 11, 1
- Schlegel, D. J., Finkbeiner, D. P., & Davis, M. 1998, *ApJ*, 500, 525
- Schmidt, M. 1968, *ApJ*, 151, 393
- Sesar, B., et al. 2006, *AJ*, 131, 2801
- Siegel, M. H., Majewski, S. R., Reid, I. N., & Thompson, I. B. 2002, *ApJ*, 578, 151
- Silk, J. 1995, *ApJ*, 438, L41
- Silvestri, N. M. et al. 2006, *AJ*, 131, 1674
- Skrutskie, M. F. et al. 2006, *AJ*, 131, 1163
- Smith, J. A. et al. 2002, *AJ*, 123, 2121
- Space Telescope Science Institute, & Osservatorio Astronomico di Torino. 2001, *VizieR Online Data Catalog*, 1271, 0
- Stobie, R. S., Ishida, K., & Peacock, J. A. 1989, *MNRAS*, 238, 709
- Stoughton, C. et al. 2002, *AJ*, 123, 485
- Tinney, C. G., Reid, I. N., Gizis, J., & Mould, J. R. 1995, *AJ*, 110, 3014
- Torres-Dodgen, A. V., & Weaver, W. B. 1993, *PASP*, 105, 693
- Tucker, D. L. et al. 2006, *Astronomische Nachrichten*, 327, 821
- van Altena, W. F., Lee, J. T., & Hoffleit, E. D. 1995, *The general catalogue of trigonometric [stellar] parallaxes* (New Haven, CT: Yale University Observatory, —c1995, 4th ed., completely revised and enlarged)
- Vanden Berk, D. E. et al. 2005, *AJ*, 129, 2047
- Vrba, F. J. et al. 2004, *AJ*, 127, 2948
- West, A. A., Hawley, S. L., Bochanski, J. J., Covey, K. R., Reid, I. N., Dhital, S., Hilton, E. J., & Masuda, M. 2008, *AJ*, 135, 785
- West, A. A. et al. 2004, *AJ*, 128, 426
- West, A. A., Walkowicz, L. M., & Hawley, S. L. 2005, *PASP*, 117, 706
- Williams, C. C. et al. 2002, *Bulletin of the American Astronomical Society*, 34, 1292
- Wolf, V. M., & Wallerstein, G. 2005, *MNRAS*, 356, 963
- Worthey, G., & Lee, H. . 2006, *astro-ph/0604590*
- York, D. G. et al. 2000, *AJ*, 120, 1579